Quantifying Asthenospheric and Lithospheric Controls on Mafic Magmatism across North Africa

P. W. Ball[1], N. J. White[1], A. Masoud[2], S. Nixon[1], M. J. Hoggard[3], J. Maclennan[1], F. M. Stuart[2], C. Oppenheimer[4] & S. Kröpelin[5]

[1]Bullard Laboratories, Department of Earth Sciences, University of Cambridge, Madingley Rise, Madingley Road, Cambridge, CB3 0EZ, UK.
[2]Scottish Universities Environmental Research Centre, Rankine Avenue, Glasgow, G75 0QF, UK.
[3]Department of Earth & Planetary Sciences, Harvard University, 20 Oxford Street, Cambridge, MA 02138, USA.
[4]Department of Geography, University of Cambridge, 20 Downing Place, Cambridge, CB2 1QB, UK.
[5]Institute of Prehistoric Archaeology and African Archaeology, University of Cologne, Jennerstraße. 8, 50823, Cologne, Germany.

Key Points:

- Analyses of 224 samples of Neogene and Quaternary igneous rocks from Libya and Chad are presented
- Geochemical and seismic estimates of asthenospheric temperature show that Haruj swell is hotter than Tibesti swell
- Combination of warm asthenosphere and thinned lithosphere generates regional uplift of North African swells

Corresponding author: pwb32@esc.cam.ac.uk, njw10@cam.ac.uk

Abstract

African basin-and-swell morphology is often attributed to the planform of sub-plate mantle convection. Across North Africa, the coincidence of Neogene and Quaternary (i.e. < 23 Ma) magmatism, topographic swells, long wavelength gravity anomalies, and slow shear wave velocity anomalies within the asthenosphere provides observational constraints for this hypothesis. Admittance analysis of topographic and gravity fields corroborates the existence of sub-plate support. To investigate quantitative relationships between intraplate magmatism, shear wave velocity, and asthenospheric temperature, we collected and analyzed a suite of 224 lava samples from Tibesti, Jabal Eghei, Haruj, Sawda/Hasawinah and Gharyan volcanic centers of Libya and Chad. Forward and inverse modeling of major, trace, and Rare Earth elements were used for thermobarometric studies and to determine melt fraction as a function of depth. At each center, mafic magmatism is modeled by assuming adiabatic decompression of dry peridotite with asthenospheric potential temperatures of 1300–1360°C. Surprisingly, the highest temperatures are associated with the low-lying Haruj volcanic center rather than with the more prominent Tibesti swell. Our results are consistent with earthquake tomographic models which show that the slowest shear wave anomalies within the upper mantle occur directly beneath the Haruj center. This inference is corroborated by converting observed velocities into potential temperatures, which are in good agreement with those determined by geochemical inverse modeling. Our results suggest that North African volcanic swells are primarily generated by thermal anomalies located beneath thinned lithosphere.

1 Introduction

Neogene and Quaternary intra-plate volcanism is widespread across North Africa. This volcanism includes the Cameroon Line, Aïr, Hoggar, Tibesti, Libya, and Darfur volcanic provinces. Magmatism is generally associated with broad topographic swells and positive long wavelength free-air gravity anomalies, which suggest a co-genetic relationship [Figure 1a-b; *Cox*, 1989]. Since the African continent is surrounded by passive continental margins with little evidence for significant horizontal shortening, it is generally assumed that swell distribution is related to the pattern of mantle convection beneath the lithospheric plate [*Burke*, 1996]. This view is corroborated by earthquake tomographic models, which show that these volcanic swells are underlain by slow shear-wave velocity anomalies [Figure 1c; *Fishwick*, 2010; *Priestley and McKenzie*, 2013; *Schaeffer and Lebedev*, 2013; *French and Romanowicz*, 2014]. Slow velocity anomalies are generally associated with elevated mantle temperatures.

The best-known volcanic swells in North Africa are Hoggar and Tibesti. These swells are thought to have developed from Eocene times until the present day with the possibility that onset of domal growth preceded volcanism [*Burke and Gunnell*, 2008; *Rudge et al.*, 2015]. They are widely regarded as iconic examples of intraplate hotspots or plumes [*Courtillot et al.*, 2003]. The less well-known Libyan volcanic field is located between Tibesti and the Mediterranean coastline. It has probably been active for the last $\sim$ 25 Ma and consists of five major provinces that have a combined areal extent of $\sim 75,000$ km^2 (Figure 2). The bulk of Libyan volcanism is aligned approximately northwest-southeast and is situated within or adjacent to the Sirt Basin, which was generated by Early Cretaceous rifting followed by thermal subsidence and Paleogene fault reactivation [*Abadi et al.*, 2008; *Abdunaser and McCaffrey*, 2015]. This basin consists of numerous northwest-southeast trending horst and graben structures that are draped by Eocene to Miocene post-rift strata. At the present day, the Sirt basin is tilted northeastwards such that its southwestern edge is partially exhumed [*Hassan and Kendall*, 2014]. The timing of this tilting coincides with a period of mild shortening in Middle Miocene times that has been linked to both development of the Libyan volcanic field and to ongoing oblique collision of the African and Eurasian plates [*Abdunaser and McCaffrey*, 2015; *Bosworth*, 2008].

Many Libyan volcanic centers are thought to be aligned with planes of inferred crustal weakness [*Bosworth*, 2008; *Elshaafi and Gudmundsson*, 2016]. The association between volcanism and rift structures of the Sirt Basin has been interpreted as evidence that a combination of lithospheric thinning and fault reactivation is the prime cause of Libyan magmatism [*Lustrino et al.*, 2012; *Radivojević et al.*, 2015]. This thinning permits adiabatic decompression of asthenospheric material, which undergoes melting at shallow depths. However, there is little evidence of post-Eocene extensional normal faulting within the basin [*Abadi et al.*, 2008]. For this reason, alternative models which combine mild lithospheric thinning with elevated mantle temperatures have also been proposed [*Beccaluva et al.*, 2008; *Cvetković et al.*, 2010; *Bardintzeff et al.*, 2012; *Lustrino et al.*, 2012; *Radivojević et al.*, 2015; *Elshaafi and Gudmundsson*, 2016].

In this contribution, our principal aim is to shed light on the origin of magmatism associated with the Tibesti and Libyan volcanic fields by calculating depths and temperatures of mantle melting from the geochemistry of mafic igneous lavas. The geochemistry of a melt formed from any single source composition depends upon the depth and temperature of melting [*Klein and Langmuir*, 1987; *McKenzie and Bickle*, 1988]. At typical mid-oceanic ridges, melt is generated as a result of passive upwelling of ambient asthenospheric mantle, which has a potential temperature of $T_p \sim 1320 \pm 20$°C [*Katz et al.*, 2003; *Herzberg et al.*, 2007; *McKenzie and Bickle*, 1988]. Beneath continental lithosphere, the amount and composition of melt is determined by the thickness of the plate, by the temperature of the asthenospheric mantle, and by the source composition. For anhydrous lherzolite at ambient asthenospheric temperatures to melt, it must upwell by adiabatic decompression to depths less than 80 km [*Jennings and Holland*, 2015; *Katz et al.*, 2003; *McKenzie and Bickle*, 1988]. When lithospheric thicknesses exceed 80 km, higher values of T_p are required to initiate decompression melting. Our secondary aim is to investigate the quantitative relationship between depth and temperature of mantle melting and the geophysical framework of North Africa. This relationship is explored by combining our geochemical insights with published earthquake tomographic models and with spectral analysis of the topographic and gravity fields. In this way, we hope to shed light upon the spatial and temporal evolution of upper mantle processes.

This observationally-based North African study is divided into three parts. First, we present the results of admittance analysis which help to determine the flexural rigidity of the lithospheric plate as well as the degree to which long wavelength topography is supported by sub-lithospheric density anomalies. Secondly, we present and analyze an inventory of major and trace elements from the five volcanic fields. Different forms of sample screening are used to mitigate the effects of crystal fractionation, of lithospheric contamination, and of source heterogeneity. Forward and inverse modeling of screened analyses are used to constrain the depth and degree of sub-lithospheric melting. Thirdly, we combine these geochemical results with shear wave velocity measurements from tomographic models to constrain mantle potential temperatures in two different ways. Thus a new framework for understanding the origin of North African volcanic swells and their wider significance is developed.

2 Admittance Analysis

A series of large topographic swells occur across North Africa. These volcano-capped swells have elevations of ~ 1 km and diameters of ~ 1000 km. They coincide with positive long wavelength free-air gravity anomalies that have peak amplitudes of ~ 50 mGal (Figure 1). Hoggar and Tibesti are the most prominent of these swells. One straightforward way to investigate their mechanism of support is to analyze the spectral relationship between the topography and gravity fields. Typically, short wavelength loads generated by surface topography are flexurally supported by the strength of the lithosphere. Longer wavelength features can be supported either by lithospheric isostasy or by sub-plate density anomalies generated by convective flow within the underlying mantle. The wavelength at which the transition from flexural to isostatic or dynamic support occurs is governed by the elastic thickness, T_e.

Admittance, $Z(k)$, is the ratio between topography and coherent free-air gravity anomalies as a function of wavenumber, $k = 2\pi/\lambda$. Here, observed values of Z are calculated within a 2900×1600 km box encompassing the classic volcanic swells of North Africa using a two-dimensional multi-taper method [*McKenzie and Fairhead*, 1997]. A large box yields more reliable estimates of admittance at longer wavelengths [*Crosby*, 2007]. We exploited SRTM30_plus topographic and satellite-derived DIR-R5 gravity fields [*Becker et al.*, 2009; *Bruinsma et al.*, 2013]. A lack of ground-based gravity measurements across North Africa means that short wavelength variations are unconstrained. The lowest satellite orbit height during the final year of the GOCE mission is ~ 200 km, which means that there is minimal power within the DIR-R5 model for wavelengths of ≤ 250 km. At the longest wavelengths, Z is 40 ± 10 mGal km^{-1}. It steadily increases to 84 ± 7 mGal km^{-1} at wavelengths of 250 km before dropping away as power is lost from the gravity model (Figure 3c). The value of coherence ranges from 0.4–0.6 over the chosen range of wavelengths, yielding reliable estimates of Z (Figure 3e).

The rapid decrease in Z over intermediate to longer wavelengths (i.e. 250–400 km) can be used to estimate the elastic thickness, T_e. Theoretical curves of admittance are calculated for a suite of values of T_e using an idealized two-layer crustal model overlying a mantle half-space. The upper and lower crust are assigned thicknesses of 15 km and 20 km, and densities of 2.4 Mg m^{-3} and 2.7 Mg m^{-3}, respectively. T_e and the fraction of internal loading that correlates with surface topography, F_2, are co-varied until a satisfactory fit between observed and calculated admittance is obtained [*McKenzie*, 2003]. A parameter sweep through $T_e - F_2$ space reveals a well-defined global minimum at $T_e = 16.6 \pm 1.5$ km and $F_2 = 3\%$. This value is broadly consistent with the results of *McKenzie* [2010] who obtained a slightly higher elastic thickness of 23 km by performing admittance analysis within a larger box that included the West African craton. It is also consistent with the results of *Audet* [2014], who explored a range of Bouguer coherence and free-air admittance schemes and recovered values of 10–70 km with an uncertainty of > 30 km for Tibesti and Haruj.

The value of T_e controls the maximum wavelength over which loads can be supported by flexural isostasy. For a line load sitting upon an unbroken plate, the distance between the location of the load and the crest of the forebulge, x_b, is given by

$$x_b = \left[\frac{4\pi^4 E T_e^3}{12g(1-\sigma^2)(\rho_m - \rho_i)} \right]^{\frac{1}{4}}, \tag{1}$$

where $E = 70$ GPa is Young's modulus, $g = 9.81$ m s^{-2} is gravitational acceleration, $\sigma = 0.25$ is Poisson's ratio, $\rho_m = 3.3$ Mg m^{-3} is the density of the mantle, and ρ_i is the density of infilling material [*Gunn*, 1943]. For air-loaded topography (i.e. $\rho_i = 0$), $T_e = 16.6 \pm 1.5$ km yields $x_b = 107^{+11}_{-10}$ km. This value is significantly smaller than half the diameter of the Tibesti swell, which suggests that these volcanic swells are not flexurally supported. A small value of T_e is consistent with pressure-temperature estimates for mantle xenoliths from the Gharyan region and from the Waw-en-Nammus volcano, which equilibrated at depths of ~ 50 km with temperatures of 890–1060 °C and 855–972 °C, respectively [Figure 2; *Beccaluva et al.*, 2008; *Miller et al.*, 2012]. Thus elastic thickness is likely to be below 35 km and North African topographic swells are probably supported either isostatically, by thickness and density variations in the lithosphere, or dynamically, by thermal buoyancy and mantle flow beneath the lithosphere.

In the absence of dynamic support, Z should decrease to zero with increasing wavelength. Instead, our results show that Z has finite values of 30–60 mGal km^{-1} at long wavelengths > 400 km (Figure 3c). These values suggest that swell elevation is maintained by sub-plate mantle convection [*McKenzie et al.*, 1973; *Colli et al.*, 2015]. At long wavelength, Z can be matched using an admittance relationship calculated for a thermal anomaly as a function of elastic thickness and of the depth to the lithosphere-asthenosphere boundary [*McKenzie*, 2010]. At wavelengths of > 350 km, the optimal model yields $T_e = 22^{+3}_{-6}$ km for a lithospheric thickness of 60 km. This value of T_e is consistent with our previous estimate and suggests that long wavelength admittance observations are accounted for by the presence of sub-plate density anomalies.

3 Magmatism

A substantial and comprehensive database of Neogene and Quaternary mafic igneous rocks was collectively assembled by us during a series of Libyan and Chadian field campaigns between 2008 and 2017 (Figure 2). Sampling strategies were designed to maximize spatial coverage across this part of North Africa where five distinct volcanic provinces have been identified: Gharyan, Sawda/Hasawinah, Al Haruj al Aswad (referred to here as Al Haruj) and Waw-en-Nammus, Jabal Eghei (also known as Jabal Nuqay), and Tibesti. Samples were analyzed for major and trace elements together with selected isotopes using X-ray fluorescence (XRF) and inductively coupled plasma mass spectrometry (ICP-MS). The resultant database consists of 224 whole rock XRF and ICP-MS analyses, 11 Sr-Nd-Pb measurements and 9 ^{3}He/^{4}He isotopic analyses. These analyses, together with details of standards and procedures, are documented in Supplementary Information [*Eggins et al.*, 1997; *Fitton et al.*, 1998; *Galer and Abouchami*, 1998; *Jochum and Nohl*, 2008; *Olive et al.*, 2001; *Tanaka et al.*, 2000; *Williams et al.*, 2005]. Where appropriate, our analyses have been supplemented by previously published information [*Beccaluva et al.*, 2008; *Bardintzeff et al.*, 2012; *Gourgaud and Vincent*, 2004; *Lustrino et al.*, 2012; *Miller et al.*, 2012; *Radivojević et al.*, 2015].

3.1 Gharyan and Sawda/Hasawinah Provinces

The Gharyan volcanic field is the northernmost and smallest province. It has an area of $\sim 3.5 \times 10^3$ km^2, comprising weathered plateau basalts, basanites and volcanic cones together with phonolite and trachytic intrusive plugs [Figure 2, *Piccoli*, 1970; *Ade-Hall et al.*, 1975a]. The age range of Gharyan activity is only partially constrained. Several basaltic flows have ^{40}K/^{40}Ar dates of 55–50 Ma and 6–2 Ma with trachytic and phonolitic plugs dated at 41–38 Ma [*Piccoli*, 1970; *Ade-Hall et al.*, 1975a].

The Sawda field has a minimum areal extent of $\sim 6 \times 10^3$ km^2 and may have been as large as 10^4 km^2 prior to erosion [*Busrewil and Esson*, 1991]. The adjacent Hasawinah field covers $\sim 10^3$ km^2. The Sawda field consists of alkaline basalts, basanites and tholeiites while the Hasawinah field has both phonolitic intrusive plugs and basaltic flows [*Busrewil and Oun*, 1991; *Busrewil and Esson*, 1991; *Oun*, 1991]. Whole rock ^{40}K/^{40}Ar dating suggests that magmatic activity in the Hasawinah field comprises phonolitic intrusions and basaltic cones which are 25–15.7 Ma [*Jurák*, 1978]. The Sawda province has ^{40}K/^{40}Ar ages of 15.5–8.5 Ma [*Schult and Soffel*, 1973; *Ade-Hall et al.*, 1975b; *Busrewil and Esson*, 1991].

3.2 Al Haruj Province and Waw-en-Nammus Volcano

The Al Haruj province is the largest of the Libyan volcanic fields and it is the only one that straddles the edge of the Sirt basin. It has been suggested that the distribution of volcanic centers across this region is controlled by crustal fractures [*Cvetković et al.*, 2010; *Elshaafi and Gudmundsson*, 2016]. For example, 84 volcanic vents trend WNW–ESE for distances of up to 100 km, which is consistent with the distribution of large-scale normal faulting within the Sirt basin [*Németh et al.*, 2003; *Less et al.*, 2006; *Cvetković et al.*, 2010;

Bardintzeff et al., 2012]. This volcanic field consists of a series of 10–100 m thick lava flows and has the greatest areal extent of $\sim 4.5 \times 10^4$ km^2. These flows are usually divided into six suites that can be further sub-divided into 15 units [*Klitzsch*, 1968; *Peregi et al.*, 2003; *Nixon*, 2011]. This volcanic activity occurs between 5.4 Ma and the present day. Note that the numerous monogenetic cones and satellite cones throughout the Haruj area are difficult to fit with relative stratigraphy [*Cvetković et al.*, 2010; *Peregi et al.*, 2003; *Nixon*, 2011]. In addition, extensive low relief flows probably obscure the earliest phases of volcanism. Whole rock ^{40}K/^{40}Ar dating shows that an outlying monogenetic cone at the southern end of the field is 8.1 ± 0.22 Ma [*Bardintzeff et al.*, 2012]. *Cvetković et al.* [2010] dated an outlying sample from the northwestern end at 11.8 ± 0.41 Ma, which they attributed to an earlier phase of volcanism that is chemically distinct from the six principal suites of flows. Here, we have divided this province into two phases on geochemical and chronologic grounds. Phase 1 (Haruj-P1) occurred between ∼ 8 and 2.5 Ma and consists of volcanic flows with monogenetic cones. Phase 2 (Haruj-P2) consists of two younger sets of volcanic flows that are ∼ 2.5 Ma [*Nixon*, 2011].

The solitary Waw-en-Nammus volcano is located ∼ 100 km southeast of the southern edge of the Haruj province. This volcano can be considered to be the youngest and southernmost cone of the province (Figure 2) [*Busrewil and Wadsworth*, 1982]. It is 0.2 Ma and its eruptive products are low in silica and rich in small (2–4 cm) mantle xenoliths compared with the rest of the Libyan Volcanic Field [*Bardintzeff et al.*, 2012].

3.3 Jabal Eghei and Tibesti Provinces

The Jabal Eghei province is located at the northeastern tip of the Tibesti topographic swell but is regarded as a separate entity. Despite it being a substantial volcanic province with an aerial extent of $\sim 1.2 \times 10^4$ km^2, little is known about its petrologic and geochemical setting. Exposed igneous rocks mostly consist of mildly alkaline basalts and basanites. Whole rock ^{40}K/^{40}Ar dates constrain the duration of volcanism to be between 16.1 ± 2.9 and 0.97 ± 0.68 Ma [*Radivojević et al.*, 2015]. Two distinct phases of volcanism are observed that can be geochemically characterized. The older phase (Eghei-P1) occurred between 17 and ∼ 3 Ma and the younger phase (Eghei-P2) occurred between ∼ 3 and 1 Ma [*Radivojević et al.*, 2015]. Eghei-P2 exhibits lower degrees of partial melting with a greater contribution from K-bearing phases that originate within the lithosphere [*Radivojević et al.*, 2015]. We have retained this division into two phases that has been corroborated by additional geochemical evidence.

The Tibesti volcanic field covers $\sim 3 \times 10^4$ km^2 and occupies about one third of the Tibesti Massif, a substantial mountain range straddling the Libyan-Chadian border (Figure 2). The highest peaks of this massif are exclusively volcanic and comprise the highest mountains of the Saharan Desert. The highest volcanic peak is Emi Koussi which has an elevation of 3415 m. These volcanoes cap uplifted Paleozoic and Precambrian basement rocks which crop out at elevations of up to 2000 m. Since the volcanic field is centered on a broad topographic swell, the Tibesti field is usually considered to have been generated by convective upwelling within a mantle plume [*Anderson*, 2005; *Courtillot et al.*, 2003; *Davies*, 1988; *Steinberger*, 2000]. Despite its importance, the Tibesti volcanic field has not been studied or sampled in any detail since the pioneering expeditions of the mid-twentieth century [*Deniel et al.*, 2015; *Gourgaud and Vincent*, 2004; *Vincent*, 1970; *Wacrenier et al.*, 1958]. Our reconnaissance work largely focussed upon primary mapping of the volcanic massif with selected radiometric dating and analysis of evolved igneous rocks from Emi Koussi [*Permenter and Oppenheimer*, 2007]. Thus the issue of whether or not the Tibesti volcanic field represents the surface expression of a continental mantle plume remains an open one. While Tibesti is volumetrically larger than the Libyan volcanic provinces, a significant proportion (i.e. ∼ 40 %) of its eruptive products are felsic in composition. Volcanism has been active since at least 17 Ma [*Deniel et al.*, 2015]. Alkali plateau basalts are capped by composite volcanoes which produced felsic and tholeiitic lavas between ~ 8 and 5 Ma with more recent ignimbritic and alkali basaltic eruptions [*Deniel et al.*, 2015; *Gourgaud and Vincent*, 2004]. Pic Toussidé, which has fumarole activity at its summit, appears to have been active during Holocene times [*Permenter and Oppenheimer*, 2007]. Published geochemical information for Tibesti is exclusively from Emi Koussi, which was active from ~ 2.4 and 1.3 Ma [*Gourgaud and Vincent*, 2004].

4 Geochemical Analysis and Screening

Figure 4 shows that marked differences in the degree of alkalinity and of silica saturation characterize the Libyan and Chadian volcanic fields. While alkali basalts and basanites dominate, tholeiitic basalts were sampled in the Gharyan, Haruj, Eghei-P1 and Tibesti fields. With respect to Haruj samples, those from both phases of Eghei are systematically depleted in alkalis and under-saturated in silica (~ 0.5 and ~ 3 wt%, respectively). The majority of Eghei-P2 samples are basanitic with Eghei-P1 samples exhibiting both basaltic and basanitic affinity. In comparison, both Haruj-P1 and Haruj-P2 samples are dominantly basaltic. Samples from Waw-en-Nammus volcano are foiditic in composition. Since Waw-en-Nammus is regarded as a satellite volcano of the Haruj province, two foiditic samples within Haruj-P1 are probably from compositionally similar volcanic cones. Gharyan, Sawda/Hasawinah and Tibesti samples span a significant range of silica compositions from basaltic andesites to foidites. This range is indicative of significant variations in melting and crystallisation conditions. Sample classification together with composition and location are summarized in Supplementary Materials.

In order to characterize the depth and degree of melting associated with intraplate volcanism, it is necessary to identify those samples which are likely to have been generated by asthenospheric melting beneath the lithospheric plate. The purpose of this sample screening is to mitigate the effects of three factors that complicate the relationship between initial and final melt compositions. The first factor is fractional crystallization, which occurs as melts are transported toward the Earth's surface. The second factor is crustal and lithospheric contamination, through which the composition of the primitive melt can be altered. The third factor concerns the composition of the sub-plate source region that undergoes melting. Each of these factors must be carefully addressed. Our goal is to demonstrate that a combination of major, trace and isotopic measurements can be used to identify and account for the effects that these processes have on primitive melt compositions.

4.1 Crystal Fractionation Effects

For mafic igneous rocks, the degree of compositional evolution is reflected by MgO content since the most common minerals that are removed by fractionation out of the melt are olivine and clinopyroxene, which are MgO rich. As these minerals crystallize, they leave the system and the MgO content of the remaining melt is reduced. Figure 5 shows major and trace element abundances of Libyan and Tibesti samples plotted as a function of MgO concentration. It is clear that major element abundances for the Haruj-P2 samples vary systematically with MgO, which implies that crystal fractionation has exerted an important influence as these samples evolved toward their final compositions. It is straightforward to produce a model of crystallizationin order to determine which minerals crystallize to generate the compositional patterns observed in Figure 5.

Here, the Petrolog3 crystallization modeling software has been used to calculate fractionation pathways for Sample 3.2 from Haruj-P2 [*Danyushevsky and Plechov*, 2011, Figure 5f]. In this case, the model allows for crystallization of olivine, clinopyroxene and spinel (± plagioclase) phases. The Petrolog3 tool uses published melt equilibrium models for individual minerals to determine possible fractionation pathways [*Danyushevsky and Plechov*, 2011]. Equilibrium mineral phases are incrementally removed from the liquid to simulate fractionation and crystallization modeling is carried out at pressures of 1 GPa.

At high concentrations of MgO (i.e. > 8 wt%), olivine fractionation dominates and both plagioclase-present and plagioclase-absent schemes replicate the observed increases in Al_2O_3, CaO and SiO_2 concentrations, as well as the observed small decrease in FeO concentrations. Below ~ 8 wt% MgO, the observed and predicted concentration of CaO gradually decreases as a consequence of the start of crystallization of clinopyroxene ± plagioclase (Figure 5b). Below ~ 6 wt% MgO, a small increase in the concentration of SiO_2 is the result of clinopyroxene ± plagioclase crystallization becoming predominant. Notwithstanding the degree of scatter, these major elemental trends are consistently observed for the entire Libyan and Chadian database. Here we use MgO = 9 wt% as a conservative cut-off to ensure that we select samples that have predominantly experienced olivine fractionation.

4.2 General Inferences about Melt Fraction

For a constant value of MgO, systematic differences in major and trace element abundances are observed (Figure 5e). For example, samples of Haruj-P2 exhibit higher concentrations of Al_2O_3 and SiO_2 but are depleted with respect to CaO and FeO compared with the rest of the database (Figure 5a-d). Major elemental differences could be due to changes in melt fraction or due to melting/crystallization conditions. As melt fraction increases, concentration of incompatible elements within the resultant magma decreases. The rate of decrease is governed by the compatibility of each element within extant mineral phases. Since the relative concentrations of two incompatible elements changes during melting, their ratio can be used as a crude proxy for melt fraction. La partitions into the melt phase more easily than Yb, which means that low melt fractions from an equivalent source have higher La/Yb ratios. Samples of Haruj-P2 have the lowest observed La/Yb values of 9.5 ± 2.6, which is consistent with the highest melt fraction.

In contrast to Haruj-P2, foiditic and basanitic samples from the Gharyan, Haruj-P1, Waw-en-Nammus and Eghei-P2 regions are undersaturated in silica, enriched in alkalis, and have high ratios of La/Yb. Apart from Gharyan samples, rocks with La/Yb > 20 do not have MgO values < 9 wt% (Figure 5e). This observation implies that more evolved melts could have stalled within the crust and generated the phonolitic intrusions observed at Gharyan and Sawda/Hasawinah. Samples from Haruj-P1, Eghei-P1 and Tibesti have a larger range of La/Yb ratios compared with Haruj-P2. Trends of major elements as a function of MgO are most clearly defined for Haruj-P2 samples since a smaller spread of melt fraction ensures that melts fractionate in a similar way. Thus major element variations at constant MgO values together with any inferences made about melt fraction observed throughout the region could result either from temperature, from pressure, or from compositional heterogeneity within the source region.

Trace element distributions of Libyan and Chadian samples strongly resemble those of Ocean Island Basalts (OIBs), which form at intra-plate settings on oceanic lithosphere (Figure 6). Their geochemical and isotopic variability is generally attributed to sub-lithospheric processes since youthful oceanic lithosphere is less likely to have isotopic variability inherited from previous melting events, compared with continental lithosphere. Intra-plate continental basalts which geochemically resemble OIBs are probably also formed by decompression melting of asthenospheric material that has not undergone significant previous depletion (e.g. at mid-oceanic ridges). Thus differences in average trace element profiles of Cenozoic volcanic fields from North Africa can be accounted for by differing degrees of fractional melting of a relatively homogeneous OIB-like source. Samples from Haruj-P1 samples have the largest range of trace element enrichment. Here, each monogenetic cone represents a discrete magmatic event, which may contribute to the greater geochemical variability compared with other volcanic fields. Enriched samples from Haruj-P1 have similar trace element distributions to samples from the Gharyan, Sawda, Waw-en-Nammus and Eghei-P2 fields and display systematically higher concentrations of incompatible elements compared with the Haruj-P2, Eghei-P1 and Tibesti fields.

4.3 Source Contributions

4.3.1 General Isotopic Constraints

Figure 7 presents 11 new isotopic analyses from the Haruj and Waw-en-Nammus regions together with previously published analyses from Gharyan and Waw-en-Nammus [see Supplementary Material; *Bardintzeff et al.*, 2012; *Beccaluva et al.*, 2008; *Lustrino et al.*, 2012; *Miller et al.*, 2012; *Masoud*, 2014]. The principal source compositions are referred to as enriched mantle 1 (EM1), enriched mantle 2 (EM2), high μ (HIMU), depleted mid-ocean ridge mantle (DMM) and common mantle reservoir (CMR), focal zone reservoir [FOZO; *Zindler and Hart*, 1986; *Stracke et al.*, 2005; *Lustrino and Wilson*, 2007]. EM1 is thought to be an inferred average for the lower crust while EM2 may represent the composition of assimilated upper crustal material. HIMU is probably a specific plume source with a high ^{238}U/^{204}Pb component. DMM may be the composition of asthenosphere that has undergone extensive melting, such as the depleted mantle beneath mid-oceanic ridges. CMR is probably the average composition of OIB-like European and North African volcanism, which includes previously published Libyan samples. FOZO is often regarded as the principal mantle component of OIB rocks. In some cases, distinct mantle sources can be easier to discriminate from each other using Pb systematics rather than ^{87}Sr/^{86}Sr or ^{143}Nd/^{144}Nd ratios. For example, HIMU is more enriched in ^{206}Pb/^{204}Pb and in ^{207}Pb/^{204}Pb compared with CMR and DMM (Figure 7c-e).

Isotopic compositions of Libyan samples reveal ^{87}Sr/^{86}Sr and ^{143}Nd/^{144}Nd ratios that range from 0.7031–0.7081 and 0.5128–0.5130, respectively (Figure 7). The Haruj and Gharyan provinces have a similar spread of ^{87}Sr/^{86}Sr values although Gharyan samples generally exhibit more enriched values of ^{143}Nd/^{144}Nd and Pb isotopic concentrations. Gharyan samples have higher values of ^{206}Pb/^{204}Pb, ^{207}Pb/^{204}Pb and ^{208}Pb/^{204}Pb (i.e. 19.5 ± 0.1, 15.7 ± 0.01, 39.315 ± 0.085) compared with Haruj samples (i.e. 19.211 ± 0.131, 15.631 ± 0.01, 38.879 ± 0.133). The Waw-en-Nammus volcanic edifice has the lowest value of ^{87}Sr/^{86}Sr (0.7031 ± 0.00003) and the highest value of ^{143}Nd/^{144}Nd ratios (0.51293 ± 0.00001) with Pb isotopic ratios that are similar to the Haruj field (18.994 ± 0.27, 15.605 ± 0.002, 38.74 ± 0.226).

We conclude that the bulk of Sr-Nd-Pb isotopic ratios for Libyan magmatic rocks lie close to, or within, mantle reservoirs that are thought to represent OIB sources (i.e. FOZO, CMR). ^{207}Pb/^{204}Pb and ^{208}Pb/^{204}Pb ratios are significantly lower than those expected for melting of a HIMU-style source (Figure 7c-e). It is unsurprising that these samples plot close to CMR values, given that previously published Libyan measurements contributed to this averaged source composition. Nevertheless, it is unlikely that enriched or fusible mantle is the source for Libyan volcanic rocks, unless an identical source is present beneath most European and North African intra-plate Cenozoic volcanic provinces.

4.3.2 Crustal Contamination

Libyan samples exhibit a wide range of ^{87}Sr/^{86}Sr values at relatively constant values of ^{143}Nd/^{144}Nd. This range could reflect crustal contamination. Two possible crustal contamination models are shown in Figure 7b. A bulk mixing model is solely concerned with addition of crustal material. In contrast, the assimilation and fractional crystallization (AFC) model calculates how isotopic composition changes during assimilation of wall-rock material and crystallization [*DePaolo*, 1981]. Both bulk mixing and AFC relationships depend upon source composition, fractionating phases as well as solid/melt distribution coefficients.

Figure 7b presents bulk mixing and AFC relationships between Sample 4.10a of Haruj-P2 and and the two-mica granite TbM2 from the Tibesti region [*Suayah et al.*, 2006]. Petrolog3 modeling suggests that olivine is the dominant fractionating phase until MgO reaches ~ 8 wt%. Since most of the samples used for isotopic analysis contain MgO > 8 wt%, the AFC calculation can be restricted to olivine fractionation. Partition coefficients are taken from *Gibson and Geist* [2010]. Both bulk mixing and AFC calculations predict a small decrease of ^{143}Nd/^{144}Nd with increasing ^{87}Sr/^{86}Sr.

Most of the observed values of ^{143}Nd/^{144}Nd and ^{87}Sr/^{86}Sr can be matched by assuming $<$ 5 wt% of either bulk mixing or AFC. The most ^{87}Sr/^{86}Sr enriched rock from the Haruj-P1 province (Sample 1.2) requires either $\sim$ 7 % of bulk mixing or $\sim$ 20 % of AFC, but it is an outlier. Although the spread of observed ^{87}Sr/^{86}Sr values is probably caused by crustal assimilation, absolute estimates of crustal contamination are difficult to determine. For example, granitic samples from the Tibesti region may, or may not, be representative of Libyan crust. Equally, the spread of Sr and Nd isotopic values attributed to crustal contamination is not corroborated by Pb isotopic data. We conclude that observed variations in Sr and Nd values reflect differences in source composition rather than crustal contamination.

4.3.3 Lithospheric Contamination

In order to discriminate between melting of lithospheric and asthenospheric mantle, it is helpful to consider what happens when lherzolite consisting of 40 to 90% olivine with significant orthopyroxene, lesser clinopyroxene and spinel/garnet, melts. Since K has a similar partition coefficient to Nb, Th and La during melting of these mineral phases, mafic samples generated by asthenospheric melting will have comparable K, Nb, Th and La values when normalized with respect to primitive mantle (i.e. $Nb_n/K_n \approx 1$ where subscript n indicates primitive mantle). Diagrams which show Nb_n as a function of K_n, La_n and Th_n are a helpful diagnostic tool (Figure 8). Samples from the Gharyan, Sawda, Waw-en-Nammus and Eghei-P2 fields exhibit a depleted K_n signature relative to Nb_n, Th_n and La_n values (i.e. the average Nb_n/K_n is 2.32 ± 1.19). This relative depletion of K_n is referred to as a K anomaly. Samples from Haruj-P1 and Eghei-P1 also have minor K anomalies (i.e. Nb_n/K_n = 1.43 ± 0.88 and 1.54 ± 0.28, respectively). No K anomaly is observed for Haruj-P2 basalts (i.e. Nb_n/K_n = 1.00 ± 0.17). Samples from Tibesti display a large range of Nb_n/K_n values, such that samples with low concentrations of Nb have no K anomalies whilst more enriched samples have K anomalies > 2.

It has previously been suggested that continental magmatic rocks including those from North Africa are generated by melting of an amphibole-bearing lithospheric source [*Roex et al.*, 2001; *Späth et al.*, 2001; *Thompson et al.*, 2005; *Lustrino et al.*, 2012; *Masoud*, 2014; *Radivojević et al.*, 2015]. In mafic rocks, K anomalies commonly occur when K-compatible phases, predominantly amphibole or phlogopite, are either present (but retained) in the source region or removed by subsequent crystal fractionation [*Varne*, 1970]. In this case, melting or fractionation must occur within the lithosphere since amphibole and phologopite are unstable at asthenospheric temperatures and pressures. Mafic rocks that exhibit K anomalies are often interpreted as partial melts of lithospheric amphibole-rich veins. These veins are thought to form when older small-degree asthenospheric melts freeze against the wet solidus within the lithosphere [*Bergman et al.*, 1981; *Roden et al.*, 1984]. Partially resorbed olivine and clinopyroxene xenocrysts are observed in lava flows from Haruj-P1, Eghei-P1/2 and Gharyan, all of which have K anomalies. Amphibole megacrysts are also encountered in isolated outcrops of Eghei-P2 where the largest K anomalies occur. We note that amphibole phenocrysts are mostly absent from Libyan and Chadian basalts for which there is no obvious correlation between Nb_n/K_n and MgO concentrations. It is therefore reasonable to conclude that K anomalies are probably the result of lithospheric partial melting rather than of fractional crystallization of K-rich phases.

Both melting of lithospheric material alone and/or contamination of asthenospheric melts as they rise through the lithospheric column have been postulated as causes of K anomalies. Melting models of asthenosphere and of amphibole-bearing lithosphere are shown in Figure 8. The principal mineral phases present within asthenospheric mantle have similar partition coefficients for K, Nb, La and Th, which implies that within the spinel or garnet stability fields the depth of asthenospheric melting does not significantly alter values of Nb_n/K_n and Nb_n/La_n. Samples from Haruj-P2 do not have K anomalies and their ratios can easily be reproduced by 2–10% partial melting of primitive asthenosphere (Figure 8b). The modest K anomaly observed in samples from Haruj-P1 and Eghei-P1 where $Nb_n/K_n < 2$ can be matched by mixing a minor volume of low melt fraction lithospheric melt with an asthenospheric melt. Similarly, Figure 8c and d show that the variation of Nb_n as a function of La_n or Th_n for these particular samples require 1–6% asthenospheric melting. Thus a mixing line can be drawn between Haruj-P1 and Eghei-P1 measurements and a hypothesized lithospheric melt. To reproduce trace element compositions for low K depletion samples from Haruj-P1, Eghei-P1 and Tibesti, $< 5\%$ contamination of a 1% lithospheric melt added to an asthenospheric melt is required.

The composition and mineralogy of putative lithospheric veins within the lower half of the plate will depend on the composition of the metasomatic phase, on the way in which this infiltrating phase has reacted with surrounding lithospheric material, and on the pressure and temperature conditions of emplacement [*Pilet et al.*, 2011]. When these veins subsequently melt, the composition of the resultant melt is governed by the amount of partial melting and by any subsequent fractional crystallization. Minor phases such as rutile and apatite strongly retain certain elements and so their presence within the source region can have a dramatic effect on trace element distributions between source and melt. Hence the complex genesis of amphibole-rich veins means that modeling lithospheric melting is an uncertain enterprise. Our estimate that $< 5\%$ lithospheric contamination is needed to produce the observed trace element compositions for Haruj-P1, Eghei-P1 and Tibesti is poorly constrained.

Samples from Gharyan, Sawda/Hasawinah , Haruj-P1, Waw-en-Nammus, Eghei-P2 and Tibesti with significant K anomalies (i.e. $Nb_n/K_n > 2$) are enriched in incompatible elements. To reproduce their chemical compositions by simple mixing between asthenospheric and lithospheric melts, an asthenospheric melt fraction of 2–10% is contaminated by 5–15% of a very small ($< 1\%$) lithospheric melt fraction. It is conceivable that significant amounts of small lithospheric melt fractions could build up against the wet solidus over millions of years. Alternatively, if these samples have formed by very small asthenospheric melt fractions of $< 2\%$, mixing between these asthenospheric melts and a lithospheric melt that contained minor enrichment in Nb, La and Th and negligible K would be required. This alternative hypothesis is less plausible. A simpler explanation for K-depleted but trace element enriched samples is that they represent melting of amphibole-rich lithospheric veins. The latter explanation is corroborated by the presence of abundant resorbed xenoliths and amphibole megacrysts within those samples that have significant K anomalies.

Geochemical analysis suggests that Haruj lavas have probably been generated by different processes to Gharyan and Waw-en-Nammus lavas even though they have similar isotopic compositions (Figure 7). Since amphibole-rich lithospheric veins are probably generated by small fractions of asthenospheric melt, the similarity of Sr-Nd-Pb isotopic compositions for Gharyan flows and entrained mantle xenoliths implies that these xenoliths have been metasomatized by OIB-like melts [*Beccaluva et al.*, 2008]. When a melt becomes isolated from the convecting mantle, its isotopic composition starts to diverge from that of the source region. With time, $^{143}Nd/^{144}Nd$ values of the now frozen melt decrease, $^{87}Sr/^{86}Sr$ values increase, and the concentration of ^{206}Pb with respect to ^{204}Pb rapidly increases. If Gharyan and Waw-en-Nammus samples have isotopic compositions that are similar to OIB, this metasomatic event must be recent [$<$ 150 Ma; *Pilet et al.*, 2011]. Within the Sirt basin, Cretaceous rifting thinned the lithosphere, which could have generated small amounts of asthenospheric melts that may have frozen to form metasomatic lithospheric veins. The fact that Gharyan xenoliths are isotopically similar to Haruj basalts implies that the asthenospheric mantle beneath Gharyan at that time and the present-day asthenospheric mantle beneath North Africa are compositionally similar [*Beccaluva et al.*, 2008].

4.4 Constraining Asthenospheric Source

Source composition exerts a significant influence on the petrology and geochemistry of magmatic rocks. Since melt composition is governed by the temperature and pressure at which melt equilibrates as well as by fractionation processes, it is challenging to quantify the heterogeneity of the sub-plate asthenospheric source. Although it is often assumed that the asthenosphere consists of dry garnet peridotite, subducted oceanic crust can be recycled into the asthenosphere in the form of eclogitic or pyroxenitic lithologies. Pyroxenites and eclogites are mineralogically distinct from peridotites and so melts derived from these lithologies will exhibit different elemental compositions. For example, North African mafic melts with significant K anomalies could be derived from small degree melting of a K-depleted asthenospheric source rather than by lithospheric contamination. In Figure 9, we have summarized our North African database by plotting Nb_n/K_n ratios of each volcanic field as a function of MgO for a range of oxides and trace element ratios.

For samples with MgO $\geq$ 9 wt%, there is a coherent relationship between Nb_n/K_n and major elemental compositions. K-depleted samples have lower concentrations of SiO_2 and Al_2O_3 but higher concentrations of FeO and CaO compared with samples from the Haruj-P2, Eghei-P1 and Tibesti fields. If trace element enrichment of slightly K-depleted samples is principally caused by contamination with a small-fraction melt of metasomatized lithosphere, minimal changes in major element concentrations are expected. If K anomalies are generated by lithospheric contamination, the observed major element variability must be produced by differences in equilibration conditions and in degree of melt for an identical source.

To determine whether or not observed major element concentrations can be derived from a lherzolitic peridotite source, we compare our database with a compilation of experimental partial melts, using the methodology described by *Shorttle and Maclennan* [2011]. For > 9 wt% MgO, the average composition of each volcanic field is compared to an inventory of 828 experimental melts of lherzolite, eclogite and pyroxenite. These experiments were conducted for a range of pressures and temperatures using anhydrous, hydrous and carbonated lithologies. The differences, in terms of wt% of oxide, between experimental melts and observed samples for a range of major elements (i.e. SiO_2, Al_2O_3, FeO, MgO, CaO, Na_2O, K_2O, TiO and P_2O_5) are summed to give a misfit value.

To account for its loss during fractional crystallization, olivine is added back into the average observed composition until misfit between observed and experimental values are minimized. Three optimal experimental melts for the average composition of each volcanic field are presented in Table 1. The average composition of samples from Haruj-P2 and Tibesti are similar to those generated by melting of either a lherzolitic source, or a combined lherzolitic and eclogitic assemblage. However, samples from Haruj-P1 and Eghei-P1, which have slightly elevated values of Nb_n/K_n require a more pyroxenitic source. These results can be explained in two ways: either small-scale heterogeneities exist within the sub-lithospheric mantle; or melting of the lithosphere contributes significantly toward the volume of erupted melts. If the lithospheric contribution is large enough to alter observed major element compositions, these samples could have been formed from lithospherically contaminated lherzolitic melting rather than by melting of asthenospheric pyroxenite.

Samples from Gharyan, Sawda, Waw-en-Nammus and Eghei-P2 have major element compositions that are sufficiently different from experimentally determined melts for any useful comparisons to be made. However, geochemical similarities of these volcanic fields implies a common origin. Experimental results suggest that melting of anhydrous peridotite will not produce samples with a foiditic affinity [*Dasgupta et al.*, 2010]. However, partial melting of a CO_2-enriched peridotite or of an asthenospheric pyroxenite could result in low-silica melts [*Pilet et al.*, 2011]. Both of these source lithologies are more fusible than anhydrous peridotite, and will therefore melt to a greater extent at identical pressures and temperatures. We infer that low-silica, trace element enriched samples from Gharyan, Sawda, Waw-en-Nammus and Eghei-P2 are at least partly derived from a fusible source.

If geochemical variability across North Africa results from asthenospheric heterogeneities or lithospheric melting, significant compositional differences on short spatial and temporal scales require explanation. The Waw-en-Nammus volcano is $\sim$ 100 km south of Haruj, and erupted at the same time as with Haruj-P2 activity [*Miller et al.*, 2012; *Masoud*, 2014; *Nixon*, 2011]. Since Haruj-P2 samples have no K anomalies and require a lherzolitic source composition, they can be interpreted as partial melts of asthenospheric lherzolitic material. However, the significant K anomalies and trace element enrichment observed for Waw-en-Nammus volcanic products require low volume, small degree melting of fusible mantle. It is unlikely that small degree melting of heterogeneous asthenospheric material beneath Waw-en-Nammus is coeval with large degree melting of lherzolitic asthenosphere beneath Haruj. A parsimonious explanation is that Haruj-P2 volcanism is generated by sub-plate melting of asthenosphere while Waw-en-Nammus volcanism is generated by localized melting of metasomatized lithosphere.

We conclude that Cenozoic magmatism of this region of North Africa is generated by melting of a combination of asthenospheric and metasomatically enriched lithospheric sources. In general, melts enriched with incompatible elements contain a larger component of, or are entirely derived from, lithospheric mantle. These geochemical inferences are broadly compatible with our helium isotopic constraints for Haruj. ^{3}He is incompatible during mantle melting and cannot be generated within the Earth. High ^{3}He/^{4}He ratios are therefore associated with melting of primordial mantle material. Helium isotopic concentrations have been calculated for gases trapped within olivine phenocrysts from the Haruj region (see Supplementary Materials for analytical details). The host lavas have uniformly low values of R/R$_a$ (4.5–6.2), where R/R$_a$ is ^{3}He/^{4}He normalized with respect to atmospheric ^{3}He/^{4}He. Values of 5.3–6.5 were obtained for lava flows and mantle xenoliths from the Gharyan field *Beccaluva et al.* [2008]. Both sets of values are similar to those reported from the Hoggar massif (8.6–8.9), from the Darfur region (6.6–9.2), and from the Cameroon Volcanic Line (5.15–7.14) [*Beccaluva et al.*, 2008; *Halldõrsson et al.*, 2014; *Pik et al.*, 2006]. Values of R/R_a which exceed those of MORB rocks (i.e. 8 ± 1) occur in the Afar and Red Sea regions [*Graham*, 2002; *Pik et al.*, 2006; *Halldõrsson et al.*, 2014]. Elevated R/R$_a$ values are generally interpreted to reflect the influence of deep primordial mantle. The moderate values reported from North African volcanic fields are thought to result from melting of shallow asthenospheric mantle, possibly with a contribution from sub-continental lithospheric mantle, which has an average R/R_a value of 6.1 ± 0.9 [*Gautheron and Moreira*, 2002; *Pik et al.*, 2006].

5 Petrologic Estimates of Mantle Potential Temperature

An important aim of this contribution is to determine whether passive upwelling of ambient asthenospheric mantle caused by lithospheric thinning, or emplacement of a sub-plate thermal anomaly, cause North African volcanism. For this reason, an ability to quantify the temperature and depth of melting is essential. Magmas generated by melting identical source regions at different pressures and temperatures will have different chemical compositions since melt fraction, mantle mineralogy, and element partition coefficients will all vary. Here, we apply two well-known methods for determining the potential temperature, T_p, of the source region. First, we exploit an inverse modeling strategy that enables the misfit between observed and calculated Rare Earth elemental (REE) compositions to be minimized by varying melt fraction as a function of depth for a specified source composition [*McKenzie and O'Nions*, 1991]. Secondly, we use a thermobarometric approach that depends upon the way in which major elements are partitioned during melt equilibration [*Plank and Forsyth*, 2016]. Both of these independent approaches share significant assumptions. For example, to sidestep the effects of fractionation, only samples with > 9 wt% MgO are used to estimate T_p. Both schemes have been parametrized assuming a lherzolitic mantle source and neither scheme corrects for contamination by crustal or lithospheric processes. Here, we limit our analysis to samples with $Nb_n/K_n < 2$. Note that estimates of T_p for the Haruj-P2 and Tibesti regions are probably more robust than those for the other volcanic provinces. In that sense, the T_p estimates shown on Figures 10 and 12 are presented in order of decreasing confidence.

5.1 Inverse Modeling of REE Concentrations

The way in which REEs partition into the melt phase depends on the extent and depth of melting. REEs are incompatible during asthenospheric melting, which means that their concentration in the integrated melt gradually reduces as melt fraction increases. As pressure and temperature increase, mantle mineralogy will change and so REE compatibility within the mantle varies as a function of depth. At pressures ≥ 2.1 GPa, the aluminous phase within the mantle is converted from spinel into garnet [*Jennings and Holland*, 2015]. Heavy REEs (eg. Yb, Lu) are much more compatible in garnet than in spinel so that the relative concentrations of light and heavy REEs within the melt are sensitive to depth of melting. If an observed REE distribution requires melting in both the spinel- and garnet-lherzolite fields, the proportion of light to heavy REEs can be used to constrain melt fraction as a function of depth. Here, we exploit the INVMEL-v12.0 algorithm, the original version of which was described and applied by *McKenzie and O'Nions* [1991]. This algorithm inverts REE distributions by minimizing the misfit between observed and predicted REEs to identify the optimal melt fraction as a function of depth. In the forward model, REE distributions are calculated by integrating instantaneous fractional melts at incremental depths along an isentropic decompression melting path [*White et al.*, 1992]. Cumulative melt fraction increases as pressure decreases and the top of the melting column is inferred to be the base of the lithosphere. Temperature exerts a strong influence on final melt fraction because hotter mantle crosses the dry solidus by a greater degree and generates a larger melt fraction at a given depth for any given starting composition [*McKenzie and Bickle*, 1988]. The INVMEL algorithm seeks the optimal solution by iteratively varying melt fraction as a function of depth until the root mean squared (rms) misfit between observed and predicted REE distributions is minimized. The starting distribution of melt fraction can be varied but is usually based upon an adiabatic gradient.

A minimum is sought using a conjugate gradient search routine called Powell's algorithm [*Press et al.*, 1986]. Once the optimal melt fraction as a function of depth is determined, the composition of other trace and major elements can be predicted by forward modeling. This prediction is a useful way to validating the approach. The INVMEL algorithm corrects for the effects of olivine fractionation effects after fitting REE distributions since olivine removal has a minor influence on REE concentration. Since predicted ratios of Mg/Fe are higher than observed values if fractionation is significant, this difference is used to estimate the amount of olivine fractionation. Melt fraction as a function of depth is then multipied by the factor $1/(1 - F)$ where F is the estimated weight fraction of removed crystals. The value of T_p is determined by comparing this corrected melt fraction distribution with a suite of isentropic curves for different values of T_p. The isentropic decompression melting model used to construct starting distributions of melt fraction and to determine T_p is taken from *Katz et al.* [2003]. The base of the lithosphere, where melt fraction is set to zero, and T_p can be varied in order to identify the smallest minimum misfit, although there is some negative trade-off between these two parameters.

The INVMEL algorithm relies upon independent estimates of significant parameters that include: REE partition coefficients, depth and thickness of spinel-garnet transition zone, and source composition. Here, we use partition coefficients that have been determined by the lattice strain parametrization of *Blundy and Wood* [2003]. In this parametrization, the partition coefficient of a given element is determined by the ionic charge and radius of the element, by the difference in size between an available mineral lattice site and ionic radius, and by pressure and temperature. We assume that the spinel-garnet transition zone occurs at 63–72 km, in agreement with the thermodynamic modeling of *Jennings and Holland* [2015]. In order to stabilize the inverse model, the depth of the base of the transition used here is slightly deeper than their chosen value of 68.1 km. The asthenospheric source is assumed to be made of lherzolite, which may have undergone depletion. If the source is depleted, the extent of melting required to match a given REE distribution must be smaller which means that T_p is lower. Nd and Sr isotopic ratios shown in Figure 7b suggest that North African magmatism is largely unaffected by crustal contamination. Therefore ϵNd values can be used to estimate source depletion. Here, a mixture of primitive (i.e. $\epsilon\text{Nd} = 0$) and depleted ($\epsilon\text{Nd} = 10$) mantle sources are used to match the observed value of ϵNd for each volcanic field [*McKenzie and O'Nions*, 1991]. For example, the Haruj-P2 field has an ϵNd of 4.61, which suggests a roughly equal amount of primitive and depleted mantle source. Where isotopic measurements are unavailable, ϵNd values are taken from nearby volcanic provinces. Thus Tibesti, Jabal Eghei and Sawda/Hasawinah are assigned ϵNd values from Haruj-P2, Haruj-P1 and Gharyan, respectively.

The results of inverse modeling of the seven sub-divided volcanic fields are presented in Figure 10. The observed REE concentrations are fitted by minimizing the rms misfit between observed and calculated concentrations. The subsequent forward-modeled fit to other trace element concentrations are generally within observational uncertainties. Exceptions are usually large ion lithophile and high field strength elements, such as Ba and Rb, whose concentrations are influenced by the effects of source enrichment and/or by poorly calibrated partition coefficients. It is clear that melt fraction and depth of melting vary across North Africa. To reproduce the average REE distribution of the Haruj-P2 field, a cumulative melt fraction of $\sim 8\%$ with melting of both garnet- and spinel-bearing asthenosphere (Figure 10a-c). In this case, the residual rms misfit between observed and predicted REEs is ~ 0.8. Quoted uncertainties in the estimated value of T_p are gauged from temperature values of the highest and lowest adiabatic melting paths that are intersected by the best-fitting model. To match observed concentrations of Fe and Mg, 26% of olivine is added and used to correct melt fraction as a function of depth. Comparison with isentropic melting curves suggest that $T_p = 1362.5 \pm 7.5$ °C for a lithospheric thickness of 57 km. Results for the Tibesti field show that $T_p = 1340 \pm 5$ °C for a lithospheric thickness of 59 km (Figure 10d-f). The Haruj-P1 and Eghei-P1 fields yield $T_p = 1340$ °C and $T_p = 1350 \pm 5$ °C, respectively (Figure 10g-l). Finally, the Gharyan, Sawda/Hasawinah and Eghei-P2 fields have much more enriched REE distributions that are consistent with significantly lower values of T_p: 1310 ± 5 °C, 1320 ± 5 °C and 1305 ± 5 °C, respectively (Figure 10m-u).

The robustness of these inverse modeling results is investigated by running large numbers of forward models in order to systematically investigate how different starting model assumptions affect our results. These parameter sweeps are carried out for potential temperatures of $T_p = 1300$–1450 °C and lithospheric thicknesses of $a = 40$–80 km at 1 °C and 1 km intervals, respectively. For every pair of values, the REE distribution is calculated for a melt fraction that varies with depth according to the adiabatic gradient whose position is fixed by the chosen values of T_p and a. The rms misfit, M, between the observed and calculated REE distribution is given by

$$M = \sqrt{\frac{1}{n}\sum_{i=1}^{n}\frac{(C_i^o - C_i^c)^2}{\sigma_i^2}} \tag{2}$$

where n is the number of REEs, C_i^o are the observed concentrations, C_i^c are the calculated concentrations, and σ_i are the standard deviations. The pair of T_p and a values which yield the smallest value of M are sought by parameter sweep. The acceptable tolerance is given by $M = 1.25$ times the global minimum since greater values result in calculated concentrations that visibly deviate from observed concentrations. We now wish to explore how varying the amount of source depletion, how changing the depth and thickness of the spinel-garnet transition, how varying water content of the source, and how choosing different mantle melting models affects the depth and degree of melting determined by inverse modeling (Figure 11). By exploiting the comprehensive INVMEL inversion algorithm, we estimated T_p and lithospheric thickness, a, to be 1340 ± 5 °C and 58 km, respectively. Guided forward modeling calculations where εNd = 4.61 show that $T_p = 1342^{+14}_{-8}$ °C and $a = 58^{+2}_{-2}$ km, which fall within the bounds of uncertainty of the inverse modeling results (Figure 11g). Finally, the functional form of M shown in Figure 11g indicates that there is a negative, but weak, trade-off between T_p and a, which means that observed REE distributions can be matched using either a slightly thinner plate underlain by hotter asthenosphere or a slightly thicker plate underlain by cooler asthenosphere.

The εNd value of a mafic magmatic sample is often used as a proxy for source depletion. A less depleted source has a greater concentration of incompatible elements than a depleted source, which means that a greater degree of melting is required to reduce the concentration of an incompatible element within the melt. The INVMEL algorithm assumes that the degree of depletion of the source is constrained by linear mixing of a primitive mantle source (PM; εNd = 0) and a depleted mid-oceanic ridge mantle (DMM; εNd = 10). In Figure 11a-f, the effects of varying the degree of depletion are shown for the Tibesti province. If εNd = 10, the global minimum occurs at $T_p = 1357^{+9}_{-7}$ °C and $a = 56^{+1}_{-2}$ km whereas if εNd = 0, the global minimum shifts to $T_p = 1335^{+18}_{-10}$ °C and $a = 59^{+2}_{-3}$ km. For Sawda, Hasawinah, Eghei and Tibesti, it has been necessary to assume εNd values. If our assumed values prove to be wrong then the calculated values of T_p could be in error by up to 10 °C. However, since the observed range of εNd values across Libya and Chad is < 1, there will be a negligible effect on values of T_p and a.

The depth and thickness of the spinel-garnet transition plays a critical role in constraining the variation of melt fraction as a function of depth since light and heavy REEs partition in different ways between source and melt for spinel- and garnet-bearing lherzolite. To match a given REE distribution, the relative amount of melting that occurs on either side of and across this transition is thus the strongest constraint on the values of T_p and a. Depth and thickness of the phase transition from spinel to garnet is much debated (e.g. *Green et al.*, 2012). Laboratory experiments at near-solidus temperatures suggest that this transition is temperature-dependent, occurring at 18–20 kbar for 1200 °C and at 26–27 kbar for 1500 °C [*Klemme and O'Neill*, 2000]. The thermodynamic approach of *Jennings and Holland* [2015] suggests that a shallower and narrower spinel-garnet transition occurs at 21.4–21.7 kbar, which is equivalent to 63–68 km. Furthermore, Cr and Fe^{3+} concentrations within the mantle increase spinel stability, which acts to widen and deepen the transition zone [*Macgregor*, 1970; *O'Neill et al.*, 2006; *Klemme*, 2004]. Here, we have assumed that the top of the transition occurs at 63 km, in agreement with *Jennings and Holland* [2015] but, in order to stabilize the INVMEL scheme, the base of the transition was lowered from 68 km to 72 km [*Klöcking et al.*, 2018]. In Figure 11g-i and j-l, we investigate the effects of increasing both the depth and the thickness of the transition. If its depth is increased by 5–10 km, T_p increases by 14–27 °C and a increases by 5–10 km. If the base of the transition is deepened from 64 km to 78 km, T_p increases by 5–18 °C and a increases by 0–2 km. Significantly, the difference between using the transition thickness of *Jennings and Holland* [2015] and the slightly larger thickness that we assume is minor and does not affect our principal conclusions.

Addition of water to the mantle depresses the solidus and causes small melt fractions to form beneath the dry solidus. Small amounts of water are probably present within the mantle but we have carried out inverse modeling by assuming anhydrous melting paths (Figure 10). It is important to investigate how water content of the source region influences the thermobarometric conditions that determine REE concentrations. Our starting point is the wet melting parametrization of *Katz et al.* [2003] which defines the shape of the wet solidus as a function of water percentage. Water contents of 0.014 wt% and 0.028 wt% are respectively calculated for depleted and primitive mantle sources, assuming H_2O/Ce = 200 in each case. If 0.014 wt% of water is present in the Tibesti source region, T_p and a marginally increase and decrease to 1326 °C and 55 km, respectively (Figure 11n). Note that the shape of the misfit function changes so that the negative trade-off between T_p and a weakens. More combinations of T_p and a yield acceptable misfits, which means that shallower melting becomes less prohibitive. If the percentage of water is increased to 0.028 wt%, T_p decreases to 1319^{+13}_{-18} °C and a decreases to 53^{+2}_{-2} km (Figure 11o). The rapid increase in misfit for T_p >∼ 1445 °C and T_p >∼ 1410 °C on Figure 11n and o reflects significant steepening of the wet solidus [*Katz et al.*, 2003]. Addition of water results in more melting for an equivalent lithospheric thickness, which yields lower predicted potential temperatures. The difference in melt fraction generated by hydrous and anhydrous melting is expected to decrease as melt fraction increases and water in the source region is exhausted. Therefore, hydrous melting has a greater effect for lower melt fractions.

Our final set of tests concern the choice of melting model (Figure 11p-r). In general, we have adopted the anhydrous melting parametrization developed by *Katz et al.* [2003]. Alternative melting models use a variety of empirical and thermodynamic strategies. These models often assume different adiabatic gradients and ambient mantle temperatures, which can result in different calculated REE distributions for the same values of T_p and a. Here, we determine how our results are affected when two alternative melting schemes are used [*McKenzie and Bickle*, 1988; *Jennings and Holland*, 2015]. In both cases, T_p increases to either 1374^{+16}_{-8} °C or 1368^{+18}_{-12} °C and a increases to 61^{+2}_{-4} km or 60^{+3}_{-4} km. Note that the *McKenzie and Bickle* [1988] model uses an ambient mantle temperature of 1315 °C, which is ∼ 15 °C colder than the values used by *Katz et al.* [2003] and *Jennings and Holland* [2015].

5.2 Major Element Thermobarometry

An alternative parametrization has been developed by *Plank and Forsyth* [2016] who use an extensive compilation of experimental melt equilibration experiments to produce thermobarometric equilibration estimates based upon major element concentrations. This empirical approach relies on the fact that concentrations of major elements depend upon the pressure and temperature of equilibration. For example, the silica activity of an equilibrated melt is pressure dependent. Silica concentration negatively correlates with pressure, which means that melt generated from an identical source at a lower pressure is silica-rich relative to a melt at a higher pressure. By compiling melting experiments of peridotite that were carried out over a range of temperatures and pressures, empirical relationships between major element composition, temperature and pressure can be established. Building on the previous work of *Lee et al.* [2009], *Plank and Forsyth* [2016] used a joint least squares inversion of major element measurements from their comprehensive experimental database to refine this thermobarometric parametrisation.

Before temperature and pressures are estimated, the composition of each sample is back-calculated to obtain that of the original melt. To reduce the uncertainties associated with this extrapolation, only primitive (> 9 MgO wt%) samples are analyzed. To account for fractionation, olivine in equilibrium with the melt is incrementally added until the composition of the sample is in equilibrium with that of the mantle source. Here, we assume a mantle forsterite fraction of 0.9, which takes into account depletion by previous melting episodes. These fractionation calculations, as well as thermobarometric estimations, are influenced by the melt oxidation state, which controls the proportion of Fe^{2+} and Fe^{3+} in the melt, and by water content. $Fe^{3+}/\Sigma Fe$ ratios and water content are not available for North African samples and so their values are estimated as follows.

Within the mantle, Fe exists in two oxidation states, Fe^{3+} and Fe^{2+}. The ratio of Fe^{3+}/Fe^{2+} depends upon oxygen fugacity, fO_2, and varies globally from ~ 0.12 at mid-oceanic ridges to ~ 0.3 at subduction zones [*Brounce et al.*, 2014]. It is important to know the relative concentrations of these Fe species since only Fe^{2+} replaces Mg^{2+} during olivine-melt exchange. Higher values of $Fe^{3+}/\Sigma Fe$ lead to lower primary MgO concentrations and therefore reduced temperature and pressure estimates. The dependence upon fO_2 means that we can use another element ratio, that is also sensitive to fO_2, as a proxy for $Fe^{3+}/\Sigma Fe$ ratios. For example, V and Sc exhibit similar compatibility during fractionation and are not fluid mobile.V is redox sensitive since it occurs in multiple oxidation states (i.e. $V^{2+,3+,4+,5+}$) while Sc is redox insensitive. If fO_2 increases, the higher oxidation states of V become prevalent and V becomes increasingly incompatible in olivine whilst Sc remains invariant. Therefore V/Sc can be used as a proxy for $Fe^{3+}/\Sigma Fe$ ratios [*Lee et al.*, 2005]. V/Sc ratios of samples from the Haruj-P2 province are 9.27 ± 0.84, (i.e. $\sim 50\%$ higher than MORB which has a value of 6.7 ± 1.1; *Lee et al.*, 2005). Since MORB has a $Fe^{3+}/\Sigma Fe$ ratio of ~ 0.12, we infer that the Haruj-P2 province has a value of ~ 0.18 although we consider a range of values from 0.1 to 0.3. On a cautionary note, it remains uncertain whether or not $Fe^{3+}/\Sigma Fe$ or V/Sc ratios of basaltic samples are dependent upon the oxidation state of their source material [*Cottrell et al.*, 2009].

H_2O concentration within the melt directly affects thermobarometric estimates [*Plank and Forsyth*, 2016]. If H_2O concentration increases, the equilibration temperature of the melt equilibrates decreases. Since Ce and H_2O have similar partition coefficients during mantle melting, Ce values can be used to gauge H_2O concentration, provided that the H_2O/Ce of the source region can be determined. For mid-oceanic ridge and oceanic island settings where the mantle has not been enriched by aqueous fluids, $H_2O/Ce = 200 \pm 100$ within the melt [*Michael*, 1995; *Dixon et al.*, 2002]. We have used this range of values to estimate H_2O concentration from observed Ce values.

We have carried out thermobarometric estimates for samples from the Haruj-P2 and Tibesti provinces (Figure 12a-f). When $Fe^{3+}/\Sigma Fe = 0.18$ and $H_2O/Ce = 200$, these estimates fall along lines that are defined by increasing temperature and pressure. The shallowest samples have equilibrated at a pressure that corresponds to a depth of 50 km. Pressures estimates for Haruj-P2 and Tibesti correlate with Sm/Yb ratio, which is often used as a proxy for depth of melting (Figure 12b and e). Potential temperature, T_p, beneath each province is determined, following the approach described by *McNab et al.* [2018]. If each sample experienced similar source conditions, thermobarometric estimates should lie along an isentropic melting curve [*Katz et al.*, 2003]. A set of anhydrous isentropic relationships was generated for $T_p = 1200$–1600 °C at 5 °C intervals. The misfit between thermobarometric estimates and these relationships was minimized in order to identify the optimal value of $T_p \pm \Delta T_p$. For the Haruj-P2 and Tibesti provinces, we obtain $T_p = 1450^{+40}_{-40}$ °C and $T_p = 1415^{+55}_{-35}$ °C, respectively (Figure 12a and d). To match the major elemental compositions by melting at ambient mantle temperatures would require $Fe^{3+}/\Sigma Fe > 0.3$ and $H_2O/Ce > 300$ (Figure 12c and f). These large values only occur in arc settings. The melting models of *Katz et al.* [2003] used to estimate T_p in Figure 12 are anhydrous. Relatively low H_2O concentrations present in the Haruj-P2 and Tibesti samples (0.99 ± 0.15 wt% at $H_2O/Ce = 200 \pm 100$) require negligible water to be present in the source (~ 0.05 wt% at 5% melting). Using the hydrous melt paths of *Katz et al.* [2003] with 0.05 wt% water would increase estimated values of T_p by ~ 20°C.

We have also carried out thermobarometric estimates for samples from the other volcanic fields. As a result of varying degrees of lithospheric contamination, these estimates are generally less robust than those obtained for the Haruj-P2 and Tibesti provinces. We obtained $T_p = 1430^{+65}_{-35}$ °C for the Haruj-P1 field, $T_p = 1480^{+85}_{-75}$ °C for the Eghei-P1 field, $T_p = 1385^{+75}_{-15}$ °C for the Gharyan field, $T_p = 1365^{+15}_{-15}$ °C for the Sawda/Hasawinah fields, and $T_p = 1430^{+25}_{-25}$ °C for the Eghei-P2 field. The shallowest depths of equilibration for each of these provinces are all deeper than for samples from Haruj-P1 or Tibesti with the shallowest samples equilibrating at depths of 55–80 km. In order to convert different thermobarometric estimates into a single value of T_p, we assume that different samples have equilibrated at different depths along a single melting path. To test this assumption, we plot Sm/Yb, a proxy for depth of melting, against the pressure of melt equilibration (Figure 12). If this assumption holds, there will be a positive correlation, which is the case for Haruj-P2, Tibesti, Haruj-P1 and Sawda/Hasawinah. Elsewhere, this correlation is less clear and therefore recovered values of T_p are less reliable.

6 Seismic Estimates of Mantle Potential Temperature

Many earthquake tomographic models indicate that the mantle beneath the African plate is characterized by shear-wave velocity anomalies. Slow anomalies are spatially coincident with topographic swells that are usually capped by volcanic rocks and with long wavelength free-air gravity anomalies. This coincidence is significant and suggests that sub-plate temperature anomalies may play a causal role. In the mantle, shear wave velocity, V_s, is generally controlled by a range of factors including density, composition, grain size, volatile content, presence of melt and melt anisotropy. However, at sub-solidus conditions it is acknowledged that temperature exerts the dominant control [e.g. *Dalton et al.*, 2014; *Priestley and McKenzie*, 2006]. Thus shear-wave velocity anomalies can be used to calculate the thermal structure of sub-plate mantle [*Priestley and McKenzie*, 2006]. Figure 13 presents a set of vertical slices through four different earthquake tomographic models.

The SL2013sv model is a global model of upper mantle structure that exploits body and surface waves (both fundamental and higher modes with periods of 11–450 s; *Schaeffer and Lebedev*, 2013). Significantly, this particular model uses an *a priori* crustal model that is iteratively updated during the optimization process whereas other schemes include fixed *a priori* crustal models. The PM-v2-2012 model is also a global model of upper mantle structure that includes body and surface waves with periods of 50–160 s [*Priestley and McKenzie*, 2013]. In contrast, the SEMUCB-WM1 model includes whole mantle coverage that is based upon a hybrid full waveform inversion of body and surface waves with periods of 32–300 s and 60–400 s [*French and Romanowicz*, 2014]. Both PM-v2-2012 and SEMUCB-WM1 models prescribe *a priori* crustal models that are based upon the 3SMAC and Crust2.0 compilations [*Nataf and Ricard*, 1996; *Bassin et al.*, 2000]. Finally, the F2010 model is confined to the upper mantle of the African plate. It includes surface waves with periods of 50–120 s and uses the 3SMAC crustal model [*Fishwick*, 2010]. The spatial resolution of all four tomographic models relies upon the global distribution of earthquakes and stations, which in turn determine the density of great circle paths for a given continent. At upper mantle depths beneath North Africa, the spatial resolution of these tomographic models is broadly similar to that of large tracts of the southern hemisphere [*Schaeffer and Lebedev*, 2013].

Figure 13a shows a horizontal slice at a depth of 150 km through the SL2013sv model. There is a striking correlation between the distribution of Neogene volcanic rocks and negative shear wave velocity anomalies, ΔV_s. This correlation is corroborated by the pattern of long wavelength free-air gravity anomalies (Figure 13b). Vertical slices through the four tomographic models that transect the principal volcanic provinces of Aïr, Hoggar, Haruj and Tibesti reveal consistent results (Figure 13c-f). ΔV_s amplitudes vary between ± 0.1 and ± 0.3 km s^{-1}, depending upon the specific reference velocity model and the degree of spatial damping used in each case. The PM-v2-2012 and F2010 models have the smallest and largest range of amplitudes, respectively. In all four models, the shear wave velocity anomalies occur immediately beneath the lithospheric plate at depths of 100–300 km. Although there is little evidence that these anomalies extend deeper into the mantle, a significant *caveat* is that as confining pressure increases and homologous temperature drops, equivalent temperature changes yield smaller changes in V_s. Furthermore, the spatial resolution of tomographic models that exploit surface waves gradually decreases with depth. The most obvious slow anomalies sit directly beneath the Hoggar and Haruj massifs where absolute shear wave velocities reach V_s = 4.2 km s^{-1}. These anomalies have consistent wavelengths of 500–1000 km on all four transects. The slow anomaly beneath the Hoggar massif almost exactly coincides with a positive gravity anomaly, whereas the slow anomaly beneath the Haruj massif is offset by ~ 500 km from a positive gravity anomaly. Although moderately slow anomalies are present beneath the Aïr and Tibesti massifs, it is striking that these anomalies are not as large as those beneath Hoggar and Haruj.

Here, we are interested in converting these ΔV_s anomalies into temperatures by applying the empirical approach pioneered by *Priestley and McKenzie* [2006] and *Yamauchi and Takei* [2016], amongst others. A number of different schemes have been used to constrain $T(V_s, P)$, none of which are based upon a detailed physical understanding of the grain boundary processes involved. One approach extrapolates the results of laboratory experiments to mantle conditions [*Faul and Jackson*, 2007]. This extrapolation upscales pressure and temperature regimes together with grain size and seismic frequency. One possible drawback of this approach is that $T(V_s, P)$ is strongly dependent upon grain size and mantle grain size is probably several orders of magnitude greater than used in laboratory experiments. A potentially more fruitful approach relies upon independent geophysical estimates of $T(V_s, P)$ to determine the relevant parameters. By combining stacked shear wave velocity models for the Pacific oceanic plate with its thermal structure obtained from the plate cooling model, it is possible to determine an empirical relationship between V_s and T [e.g. *Priestley and McKenzie*, 2006; *Richards et al.*, 2018]. This relationship can be fine-tuned using additional constraints (e.g. the mantle adiabatic gradient, mantle xenolith thermobarometry, sub-plate attenuation measurements, constraints for upper mantle viscosity; *Priestley and McKenzie*, 2013). By using this V_s to T conversion scheme for North Africa, we are implicitly assuming that the mantle beneath oceanic basins and continents behaves in a similar way. This empirical approach provides one practical means for converting V_s into T.

The resultant values of V_s as a function of temperature and pressure reveal two distinctive regimes [*Takei*, 2017]. For homologous temperatures (i.e. ratio of the temperature of a material, T, to that of its melting point, T_m, both measured in Kelvin) of $T/T_m < 0.92$, the relationship between V_s and T is approximately linear, as would be expected for a purely elastic medium [*Yamauchi and Takei*, 2016]. When $T/T_m > 0.92$, anelastic effects start to dominate and V_s rapidly decreases as a function of T. *Yamauchi and Takei* [2016] developed a revised anelastic model at 50 and 75 km depths that is calibrated using oceanic V_s stacks from the PM-v2-2012 model. This approach has been used to determine $T(z)$ from $V_s(z)$ beneath North Africa for the PM-v2-2012 model. The ambient potential temperature of sub-lithospheric mantle is assumed to be 1330 °C [*Katz et al.*, 2003]. Figure 14a shows the horizontal distribution of temperature at a depth of 150 km. Beneath the Hoggar and Haruj massifs, temperature anomalies of 30–40 °C are obtained that correspond to maximum potential temperatures of 1360–1370 °C. In contrast, the maximum potential temperature beneath the Tibesti massif is only 1330 °C. Note that the presence of melt within the mantle will tend to lower the value of V_s which means that the calculated temperature is overestimated. At depths > 100 km, we assume that negligible melt is present.

It is more difficult to determine lithospheric thickness from earthquake tomographic models, partly because the amplitude and wavelength of V_s anomalies at depths < 100 km can be affected by downward bleeding of crustal velocities [*Priestley and McKenzie*, 2013]. One crude estimate is obtained by mapping out the depth of, say, the 1300 °C isothermal surface (Figure 14b and c). West of the Hoggar massif, this estimate suggests that continental lithosphere thickens rapidly to values consistent with calibrated surface wave tomographic models which show that the West African cratonic lithosphere is > 200 km thick [*Priestley and McKenzie*, 2013]. Beneath the Hoggar and Haruj-Tibesti massifs, the lithosphere thins to 50 km, which is consistent with anomalously elevated heatflow measurements of 70 mW m^{-2} along the western edge of the Sirt basin adjacent to the Haruj and Sawda/Hasawinah volcanic fields [*Nyblade et al.*, 1996]. This inference is consistent with the admittance analysis presented in Figure 3.

7 Discussion

There is compelling petrologic evidence that sub-plate temperature anomalies play a significant role in generating mafic volcanism beneath the Tibesti and Haruj provinces. This inference is corroborated by earthquake tomographic models, which show that both provinces are underlain by slow shear-wave velocity anomalies at depths of 100–200 km, and by admittance analysis of the gravity and topographic fields, which implies that sub-plate density anomalies provide dynamic support. The satellite volcanic provinces of Gharyan, Sawda/Hasawinah, Waw-en-Nammus and Eghei are probably generated by modest asthenospheric temperature anomalies with compelling evidence for at least some lithospheric contamination. Here, we explore the implications of these results in three ways. First, we scrutinize our ability to obtain meaningful estimates of asthenospheric temperature from different petrologic and geochemical approaches. Secondly, we discuss the robustness of the relationship between petrologic and seismic temperature estimates. Combined with lithospheric thickness measurements, these estimates have significant implications for the generation and maintenance of regional topographic support. Finally, we use our observational results from these North African volcanic fields to sketch out the likely temporal and spatial evolution of mafic magmatism.

7.1 Comparing Different Petrologic Temperature Estimates

Numerous contributions have emphasized the importance of lithospheric thinning and fault reactivation in generating the Haruj and associated volcanic fields [*Bardintzeff et al.*, 2012; *Cvetković et al.*, 2010; *Elshaafi and Gudmundsson*, 2016; *Lustrino et al.*, 2012; *Abdunaser and McCaffrey*, 2015; *Radivojević et al.*, 2015]. This emphasis stems from the NW-SE alignment of Libyan volcanism, which strikes approximately parallel to major basement faults of the adjacent Sirt basin. This coincidence suggests that Cretaceous rift structures play a role in melt migration. An important aim of this contribution is to exploit a combination of inverse modeling of REE distributions and major element thermobarometry to show that North African volcanism, which generally has an OIB affinity, is generated by decompression melting of anomalously hot asthenospheric mantle.

Our most unambiguous results are from the Haruj-P2 and Tibesti provinces. Beneath Haruj-P2, REE modeling and thermobarometric calculations yield potential temperatures of 1362.5 ± 7.5 °C and 1450^{+40}_{-40} °C, respectively. Beneath Tibesti, REE modeling and thermobarometric calculations yield potential temperatures of 1350 ± 5 °C and 1415^{+55}_{-35} °C, respectively. We obtained respective potential temperatures of 1340 °C and 1350 ± 5 °C, and of 1430^{+65}_{-35} °C and 1480^{+85}_{-75} °C, for the Haruj-P1 and Eghei-P1 fields. However, these results may be affected to a greater extent by lithospheric contamination. In agreement with previous contributions, we found that volcanism from the Gharyan, Sawda/Hasawinah, Waw-en-Nammus and Eghei-P2 fields can be explained by a combination of asthenospheric and lithospheric melting at approximately ambient potential temperatures. *Beccaluva et al.* [2008] also suggest that a sub-lithospheric thermal anomaly played a role in generating the Gharyan volcanic field. Thus mafic samples from these fields have varying degrees of lithospheric contamination with evidence for remobilization of previously trapped amphibole-bearing veins of OIB-style melt. It is reasonable to infer that the contribution of lithospheric melts at the Gharyan, Sawda, Waw-en-Nammus and Eghei-P2 fields is well established [*Miller et al.*, 2012; *Bardintzeff et al.*, 2012; *Radivojević et al.*, 2015; *Masoud*, 2014; *Lustrino et al.*, 2012; *Beccaluva et al.*, 2008]. Some studies also favor significant contamination of rising asthenospheric melts. Subsequent phases of

Haruj volcanism represent ~ 8% partial melts of both spinel and garnet-bearing asthenosphere, whilst earlier, more enriched samples require a degree of lithospheric contamination. These inferences broadly agree with the trace element modeling results of *Cvetković et al.* [2010], who argued that the youngest samples required ~ 5% melting of a purely garnet-bearing asthenosphere. Our analysis of Tibesti samples require ~ 5% melting of both spinel- and garnet-bearing asthenosphere.

In contrast, major element thermobarometric estimates yield potential temperatures that are ~ 100 °C hotter than values calculated by inverse modeling of REE distributions. The results of both techniques indirectly suggest that melting occurs at depths of 60–100 km. There are three possible explanations for the substantial temperature discrepancies. First, both approaches suffer from numerous sources of uncertainty and trade-offs that have been discussed in this contribution. Secondly, inverse modeling of REE distributions could be significantly underestimating mantle potential temperatures. The INVMEL algorithm attempts to identify the simplest pattern of melt fraction as a function of depth that minimizes the misfit between observed and calculated REE distributions. Inevitably, a range of simplified assumptions are made about, for example, source composition and the structure of the spinel-garnet phase transition. We have carefully investigated the most important of these assumptions and conclude that there is relatively little room for manoeuvre since both the lower and upper limits of potential temperature are tightly constrained, provided that our starting assumption of a dry lherzolitic mantle source is reasonable. Furthermore, inverse modeling of REE distributions from a global suite of mid-oceanic ridge basalts yields mantle potential temperatures that are consistent with independent geochemical and geophysical estimates [e.g. $Na_{8.0}$ and crustal thickness measurements; *Dalton et al.*, 2014; *White et al.*, 1992].

It is generally accepted that a potential temperature of $T_p = 1320 \pm 20$ °C is required to generate ~ 7 km of mid-oceanic ridge basalt by decompression melting [*Katz et al.*, 2003; *Herzberg et al.*, 2007; *McKenzie and Bickle*, 1988]. Note, however, that deepening the spinel-garnet transition zone tends to increase the estimate of mantle potential temperature. Another possible explanation is that major element thermobarometric modeling, which does not include polybaric fractional melting, could be overestimating mantle potential temperatures. For mid-oceanic ridges, *Lee et al.* [2009] used thermobarometric estimates to obtain a mantle potential temperature of 1350 ± 50 °C. This value is hotter than, but within the range of uncertainty of, ambient asthenospheric mantle. Since our method of estimating T_p from thermobarometric results incorporates loss of latent heat during melting, a thermobarometric value of T_p for MORB samples will be considerably higher than that originally quoted by *Lee et al.* [2009]. Thus by fitting melting paths to thermobarometric estimates, calculated values of T_p are higher than those obtained by the INVMEL algorithm.

7.2 Linking Volcanism, Seismic Tomography and Regional Uplift

It is significant that petrologic estimates of mantle potential temperature closely agree with estimates determined by empirical calibration of earthquake tomographic models (Figure 14e). The principal difficulty in comparing petrologic and seismic temperature estimates concerns the choice of depth range over which to average the seismic estimates. Here, we found that the optimal correlation was obtained when seismically determined temperature estimates were averaged between 100 and 200 km (Figure 14e). There is also reasonable agreement between the top of the melting column estimated by both melting models and the depth of the 1300 °C isothermal surface, which is taken to be the base of the lithospheric plate (Figure 14c).

This significant result is borne out by the close geographic relationship between volcanism, tomography and free-air gravity anomalies (Figure 1b and c). Throughout North Africa, a swathe of volcanic activity reaching from Libya through Chad to the Cameroon

Volcanic Line and from Jordan through Arabia and Afar to Uganda strikingly matches the detailed distribution of slow shear wave velocities and positive free-air gravity anomalies. South of the equator, there is excellent correspondence between slow shear wave velocities, free-air gravity anomalies and volcanism for Angola, Madagascar and the Comores Islands. This coincidence between volcanism, long wavelength topographic swells and positive free-air gravity anomalies provides additional corroboration for the dynamic support of these swells [*Burke*, 1996].

The Hoggar and Tibesti topographic swells have elevations of 2–3 km with positive free-air gravity anomalies of up to 50 mGal (Figure 1a). Topography generated by sub-plate convective processes can be gauged by scaling free-air gravity anomalies with the long wavelength ($\sim$ 2000 km) admittance, $Z = 40$ mGal km^{-1} (Figure 3). This approximation suggests that, in the case of Hoggar and Tibesti, about 1 km (i.e. one half of the swell's amplitude) is generated by sub-plate processes. This simple inference breaks down to some extent when petrologic and seismic observations are considered. Although the Hoggar massif is underlain by a slow shear wave velocity anomaly, it is surprising to find that the Tibesti massif has a much smaller velocity anomaly than the relatively low-lying Haruj region, which has a velocity anomaly almost as large as that beneath Hoggar. The presence of this velocity anomaly is consistent with petrologic temperature estimates. The Haruj region has an average elevation of $<$ 500 m and a free-air gravity anomaly of $\sim$ 20 mGal which suggests that it has modest sub-plate support.

There are three possible isostatic mechanisms for generating regional uplift of a swell, U. First, the temperature within a sub-lithospheric channel can be raised. Secondly, magmatic underplating of the crust can occur. Thirdly, the lower part of lithospheric mantle can be removed (see Figure 15). The three relevant analytical relationships are given by

$$U = \frac{z_{ac}(\rho_{a,o} - \rho_{ac})}{\rho_{a,o}}, \tag{3}$$

$$U = \frac{(z_{l,o} - z_c)(\rho_{lm,o} - \rho_{lm,n}) + z_u(\rho_{a,o} - \rho_u)}{\rho_{a,o}}, \tag{4}$$

$$U = (z_{l,o} - z_c)\frac{\rho_{lm,o}}{\rho_a} - (z_{l,n} - z_c)\frac{\rho_{lm,n}}{\rho_a} - (z_{l,o} - z_{l,n}). \tag{5}$$

In each case, z and ρ refer to thicknesses and densities where subscript c indicates crust, l indicates lithosphere, lm indicates lithospheric mantle, a indicates asthenosphere, ac indicates an anomalously hot asthenospheric channel (i.e. thickness of layer that underlies plate), and u indicates magmatic underplating. Subscript o refers to the reference lithospheric column and n refers to the modified lithospheric column. The upper and lower crust are assigned thicknesses of 15 km and 20 km, and densities of 2.4 Mg m^{-3} and 2.6 Mg m^{-3}. Lithospheric and asthenospheric densities are functions of pressure and temperature. With the exception of the asthenospheric channel calculations, the sub-plate asthenosphere is assumed to have a T_p of 1330 °C, a reference density of 3.33 Mg m^{-3}, a temperature gradient of 0.6 °C km^{-1}, a pressure gradient of 0.033 GPa km^{-1}, a thermal expansion coefficient of 4x10^{-5} °C^{-1}, and a bulk modulus of 115.2 GPa. The base of the lithosphere is assigned a T_p of 1330 °C and temperature is assumed to linearly decrease to zero at the surface. These calculations ignore depletion of the lithospheric mantle. For the asthenospheric channel and magmatic underplating calculations, a lithospheric thickness of 75 km is assumed.

The gravity anomaly, Δg, for each model is calculated using the difference in mass distribution between the reference and modified lithospheric columns. These columns are assumed to comprise of a set of 1 m thick infinite slabs where

$$\Delta g = 2\pi G h \Delta\rho e^{-2\pi z/\lambda}, \qquad (6)$$

where G is the gravitational constant, $h = 1$ m is the layer thickness, z is the depth to the weighted middle of the layer, $\lambda = 1600$ km is the lateral wavelength, and $\Delta\rho$ is the density difference for a layer at depth z between the two lithospheric columns [*Crosby and McKenzie*, 2009].

A significant means for generating support is the existence of density anomalies generated by asthenospheric temperature anomalies (Equation 3; Figure 15a). Beneath the Haruj field, tomographic models reveal a slow shear wave anomaly between 100 and 200 km depth that has a temperature anomaly of $\sim$ 50 °C. Beneath the Tibesti swell, a $\sim$ 50 km thick layer with a temperature anomaly of $\sim$ 25 °C is visible. These thermal anomalies generate $\sim$ 210 m and $\sim$ 25 m of regional isostatic uplift, respectively. Equation 3 assumes that surface deflections are only sensitive to density variations above the depth of compensation (i.e. above the base of the lithospheric columns). This assumption is consistent with indirect evidence for a viscosity contrast at the base of the asthenospheric channel which implies that deformation of the Earth's surface is less sensitive to the mantle flow field generated by density anomalies beneath this viscosity contrast [*Hager and Richards*, 1989].

Magmatic underplating can produce regional uplift [*Cox*, 1993]. The Tibesti volcanic field has been active for at least 10 Ma longer than Haruj and its melt productivity is concomitantly greater [5–6 $\times 10^3$ km^3 compared with $< 1 \times 10^3$ km^3; *Deniel et al.*, 2015]. The Tibesti field also consists of substantial volcanic edifices with large quantities of evolved material. In contrast, the Haruj volcanic field comprises low-lying basaltic lava flows. Intrusion of the lower crust by gabbroic material is inferred to have occurred beneath many volcanic provinces using indirect petrologic arguments, such as fractionation of clinopyroxene at Moho pressures [*Cox*, 1993]. Since the volcanic plumbing system beneath Tibesti is longer lived and probably more extensive than that beneath Haruj, it is conceivable that magmatic underplating is volumetrically more significant. Regional uplift generated by this mechanism is $\sim$ 10% of underplate thickness [*Maclennan and Lovell*, 2002]. Assuming that $\sim$ 70% of material is trapped at depth and that the locus of underplating matches that of surface volcanism, Haruj and Tibesti may have $<$ 0.1 km and $\sim$ 0.6 km thickness of underplate, respectively. If this underplate has a density of $\sim$ 2.9 Mg m^{-3}, it will generate uplift of $<$ 10 m and $\sim$ 55 m, respectively. It is important to note that the relative proportions of magmatic material erupted and trapped at the base of the crust is poorly known and so these uplift estimates are quite uncertain [*Maclennan and Lovell*, 2002].

Removal of lithospheric mantle by, say, thermal erosion produces a significant topographic response. Lithospheric thickness estimates of 50–60 km have been obtained beneath Libya and Tibesti. Removal of 50 km of lithospheric mantle generates an initial uplift response of $\sim$ 0.65 km, increasing to $\sim$ 1 km when the lithosphere becomes thermally re-equilibrated (Figure 15b and c). In the continents, regional uplift generated by lithospheric removal dwarfs that generated by changes in asthenospheric temperature. Significant lithospheric thickness change beneath Tibesti compared to Haruj could therefore account for the observed elevation differences. It is also important to note that the Haruj province was probably erupted at lower elevations since it sits on the edge of the low-lying Sirte basin. Regional uplift generated by elevated asthenospheric temperatures, magmatic underplating and lithospheric removal will have an associated positive free-air gravity anomaly. In these examples, a positive increase in mass at the surface is balanced by a reduction in density at depth. Since the gravity response is sharply attenuated with depth, each of these uplift processes generates an increase in the size of the free-air gravity anomaly measured at the surface (Figures 15d-f).

7.3 Temporal and Spatial Patterns

The transition between Eghei P1 and Eghei-P2 occurred at ~ 4 Ma, which is roughly coeval with the transition between Haruj P1 and P2. These transitions correspond to a decrease in melting at Eghei and an increase in melting at Haruj. Only Haruj and Waw-en-Nammus have lavas that are younger than 1 Ma. Haruj and Waw-en-Nammus represent provinces that overlie a significant present-day low-velocity anomaly within the asthenosphere. It is therefore conceivable that coeval decreases and increases in melting at Eghei and Haruj are generated by flow of an asthenospheric thermal anomaly that is at present centered beneath Haruj. Relative motion between the African plate and underlying asthenospheric temperature anomalies through time may impact the geochemistry, volume and location of volcanic eruptions at the surface on short time scales.

There is evidence for large-scale northeastward stratigraphic tilt away from Libyan volcanic centers [*Conant and Goudarzi*, 1964]. A large angular discontinuity occurs at the present-day surface such that Paleocene sedimentary rocks are now exposed along western fringes of the basin, suggesting post-Miocene regional uplift [*Conant and Goudarzi*, 1967; *Abadi et al.*, 2008; *Abdunaser et al.*, 2014]. Peak oil generation occurred between Late Oligocene and Pliocene times, with northwest-southeast migration pathways that are updip of this regional tilting [*Roohi*, 1996; *Hassan and Kendall*, 2014]. The notion that post-Middle Eocene sedimentary rocks were once widespread across the basin but were subsequently tilted and removed in the west is supported by thermal maturation trends. *Gumati and Schamel* [1988] examined vitrinite reflectance in five wells and found that Upper Cretaceous shales along the western edge of the basin are overmature, given their current shallow burial depths and their estimated paleogeothermal gradient. Thermal modeling requires erosion of $>$ 1 km of overburden in Neogene times, which is a thickness equivalent to that of the Cenozoic stratigraphy in the central regions of the basin at the present day. Isostatic calculations show that ~ 250–750 m of regional uplift is required to generate the 1–3 km of denudation observed along the western edge of the Sirt basin.

Nyblade et al. [1996] analyzed heatflow measurements from 66 boreholes with measured bottom-hole temperatures and thermal conductivities constrained by drill core and cuttings. Average heat flow is 72 ± 9 mW m^{-2}, which is slightly higher than those observed for undisturbed Late Proterozic terrains (55 ± 17 mW m^{-2}). The main source of variation within the basin arise from higher values on the basement horsts and lower values within the intervening grabens. This range is probably due to either heat refraction at the sediment-basement interface or the lack of a sedimentation correction to measurements within the grabens. There is evidence for more elevated values in the western portion of the basin closer the volcanic fields. 24 heat production measurements on basement samples from wells that penetrated the entire section suggest that these heatflow measurements are not inconsistent with observed levels of crustal radioactivity. Therefore elevated asthenospheric temperatures and thinned lithosphere cannot necessarily be inferred from these observations alone.

Integrating these various observations suggests that there has been significant Neogene uplift along the western edge of the Sirt basin adjacent to the volcanic centers. Regional stratigraphic tilting to the northeast influenced hydrocarbon migration pathways, whilst erosion of uplifted sedimentary infill led to ~ 1–3 km of denudation and anomalously mature source rocks at shallow depths. The rapid removal of uplifted material from the western Sirt Basin during late Cenozoic times, coupled with differences in extent of lithospheric thinning over this period, may explain the anti-correlation between the topographic expressions and asthenospheric potential temperatures estimated beneath Haruj and Tibesti.

8 Conclusions

A comprehensive geochemical database of mafic rocks from North Africa has been assembled. Analysis and modeling of this database is used to determine the depth and degree of melting. In this study, we have also combined regional topographic, gravity and tomographic observations across North Africa with geochemical analysis of igneous rocks from the principal North African volcanic fields. Correlation between topographic swells and positive long wavelength gravity anomalies confirms that the $\sim$ 1000 km wavelength basin-and-swell topography is a surface response to mantle convection. Tomographic images reveal these topographic swells are generally underlain by anomalously hot asthenospheric mantle. The majority of North African domal swells are capped by Cenozoic volcanism. Asthenospheric potential temperatures beneath Haruj in the last 5 Ma are estimated to be $\geq$ 50°C hotter than ambient mantle using combined geochemical and earthquake tomographic modeling techniques. These temperatures are $\sim$ 20–40 °C hotter than those predicted to be present beneath the Tibesti region. To reproduce observed geochemical patterns across Libya and Tibesti requires some contribution from lithospheric melting. These lithospheric melts may represent remobilisation of OIB-style magma emplaced during Cretaceous rifting of the Sirt basin. Lithospheric thicknesses estimates from geochemical and tomographic studies suggest the plate beneath Haruj and Tibesti is anomalously thin ($\leqslant$ 60 km). Thus a combination of elevated asthenospheric temperatures and lithospheric thinning seems to have generated melting beneath North Africa. Similarities between the Libyan and Tibesti volcanic fields and other areas of North African volcanism suggest similar processes could also be responsible for these features.

Table 1. Analysis of average composition of each volcanic field with melt compositions calculated using experimental database of *Shorttle and Maclennan* [2011]

Misfit (wt%)	Material	Lithology	P(GPa)	T (°C)	F (%)	Reference
Haruj P2						
3.36	GA1 MPY90 mix	lrz$_a$+ecl$_a$	3.5	1500	−1	*Yaxley and Green* [1998]
3.81	KPS3.2	lhz$_a$	3.0	1430	31.9	*Davis and Hirschmann* [2013]
3.85	KLB1	lhz$_a$	4.6	1750	22.0	*Takahashi et al.* [1993]
Haruj P1						
4.32	Pyrox2B	px$_a$	1	1300	11.0	*Kogiso et al.* [2001]
4.83	OLCPX1	px$_a$	1	1300	14.0	*Kogiso et al.* [2001]
4.86	MIX1G 95mmh05	px$_a$	2.0	1400	26.0	*Kogiso et al.* [2003]
Eghei P1						
2.95	77SL-582–378	px$_a$	2.0	1370	18.1	*Keshav et al.* [2004]
3.04	77SL-582–369	px$_a$	2.5	1360	34.8	*Keshav et al.* [2004]
3.12	77SL-582–377	px$_a$	2.0	1400	42.2	*Keshav et al.* [2004]
Tibesti						
2.04	GA1 MPY90 mix	lrz$_a$+ecl$_a$	3.5	1500	−1	*Yaxley and Green* [1998]
3.26	GA1 MPY90	lrz$_a$+ecl$_a$	3.5	1300	−1	*Yaxley and Green* [1998]
3.31	OLCPX1	px$_a$	1.0	1300	14	*Kogiso et al.* [2001]

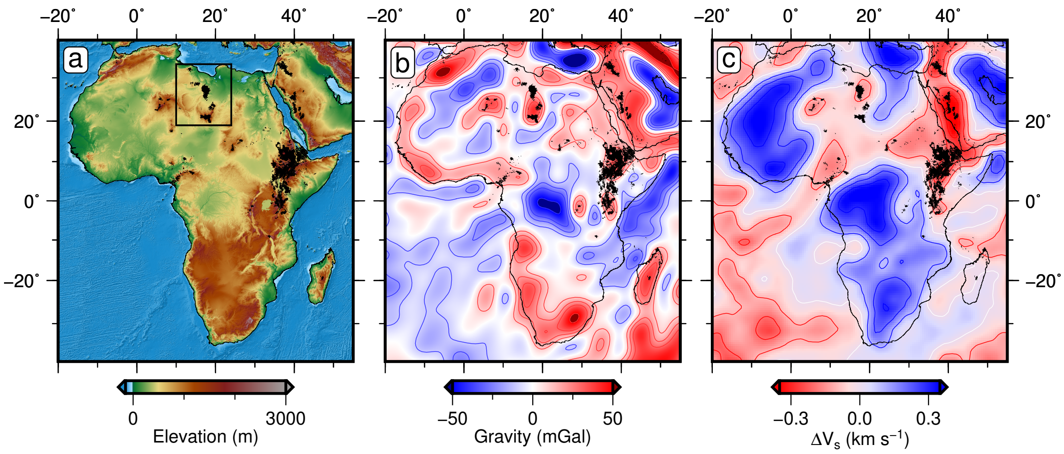

Figure 1. (a) Topographic map of Africa and Arabia showing distribution of Neogene and Quaternary volcanic rocks. Black patches = volcanic fields < 30 Ma. Box = portion of North Africa displayed in Figure 3. (b) Long wavelength (i.e. > 800 km) free-air gravity map calculated from DIR-R5 database [*Bruinsma et al.*, 2014]. Red/white/blue contours = positive/zero/negative values plotted at intervals of 10 mGal. (c) Map showing horizontal slice through SL2013sv shear wave tomographic model at depth of 150 km [*Schaeffer and Lebedev*, 2013]. Red/white/blue contours = positive/zero/negative values of shear wave anomalies plotted at intervals of 0.1 km s^{-1}.

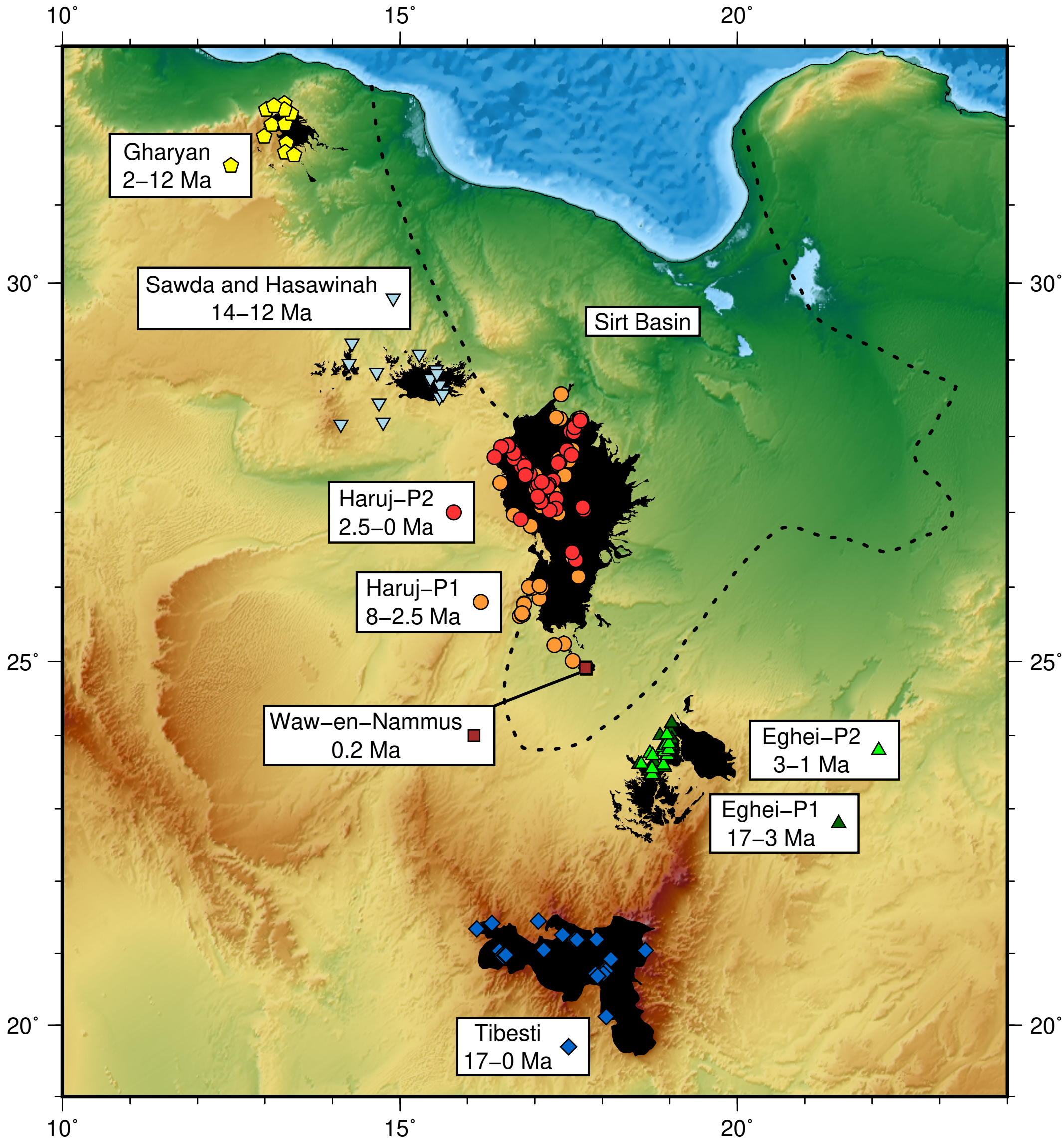

Figure 2. Topographic map of central portion of North Africa showing distribution of Neogene and Quaternary volcanic rocks from Libya and Chad (see Figure 1 for location). Black patches = volcanic fields < 30 Ma; colored circles = loci of volcanic samples described and analyzed in this study; labeled boxes = names of individual volcanic fields with ranges of radiometric dates taken from *Ade-Hall et al.* [1975a], *Bardintzeff et al.* [2012], *Busrewil and Esson* [1991], *Cvetković et al.* [2010], *Deniel et al.* [2015], *Jurák* [1978], *Masoud* [2014], *Radivojević et al.* [2015] and *Schult and Soffel* [1973]; dotted line = outline of Sirt Basin taken from *Abdunaser and McCaffrey* [2015].

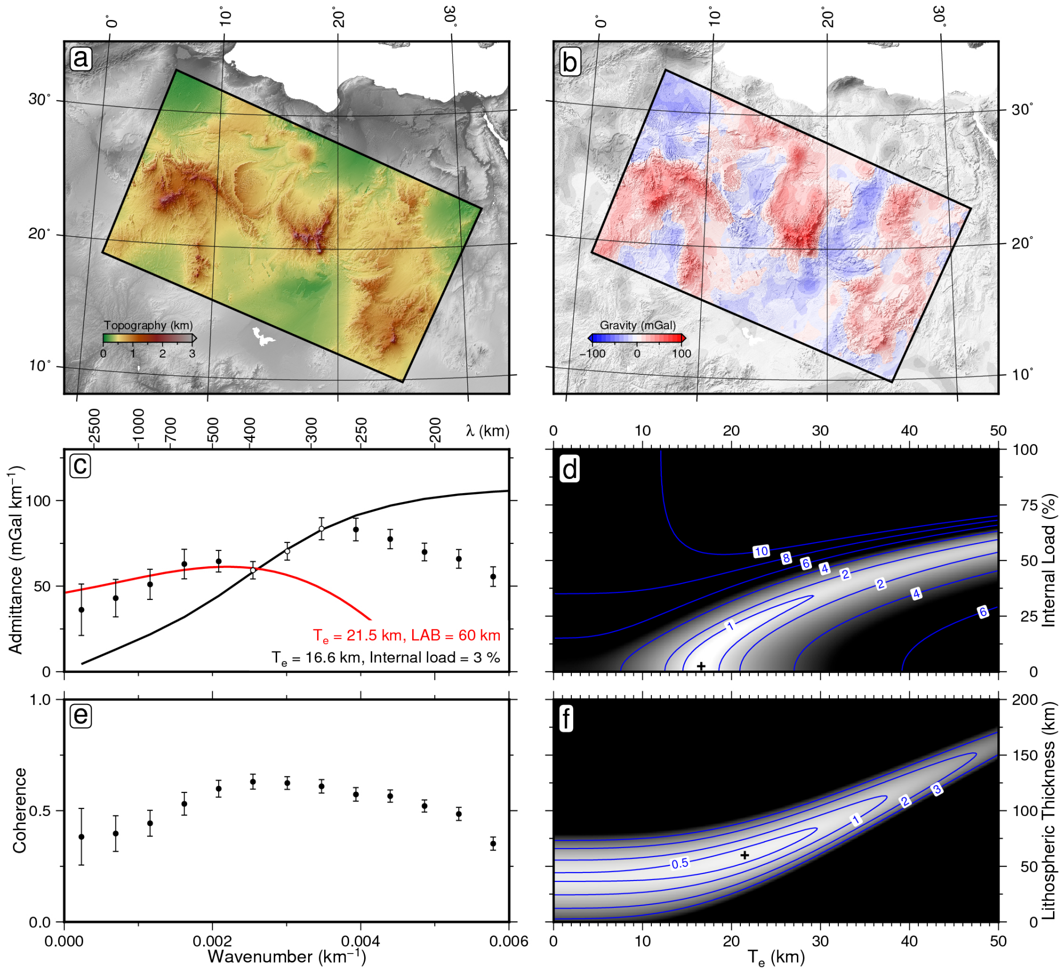

Figure 3. (a) Digital topography extracted from *SRTM30_PLUS* database [*Becker et al.*, 2009]. Box = 2900 × 1600 km window of analysis. (b) Free-air gravity anomalies extracted from *DIR-R5* database [*Bruinsma et al.*, 2014]. Box as before. (c) Admittance analysis. Circles with vertical bars = observed admittance values $\pm 1\sigma$ plotted as function of wavenumber; open circles = observed values used to constrain elastic model; black line = best-fitting elastic model where T_e = 16.6 km and internal load = 3%; upper/lower crustal thicknesses and densities are 15/20 km and 2.4/2.7 Mg m^{-3}, respectively; red line = Predicted dynamic support calculated using method of *McKenzie* [2010] where T_e = 21.5 km and thickness of mechanical lithosphere = 60 km. (d) Residual misfit plotted as function of elastic thickness and internal load percentage. Black cross = locus of global minimum. (e) Coherence between topographic and gravity signals plotted as function of wavenumber. (f) Residual misfit between observed and predicted dynamic support for wavelengths > 350 km plotted as function of elastic thickness and lithospheric thickness.

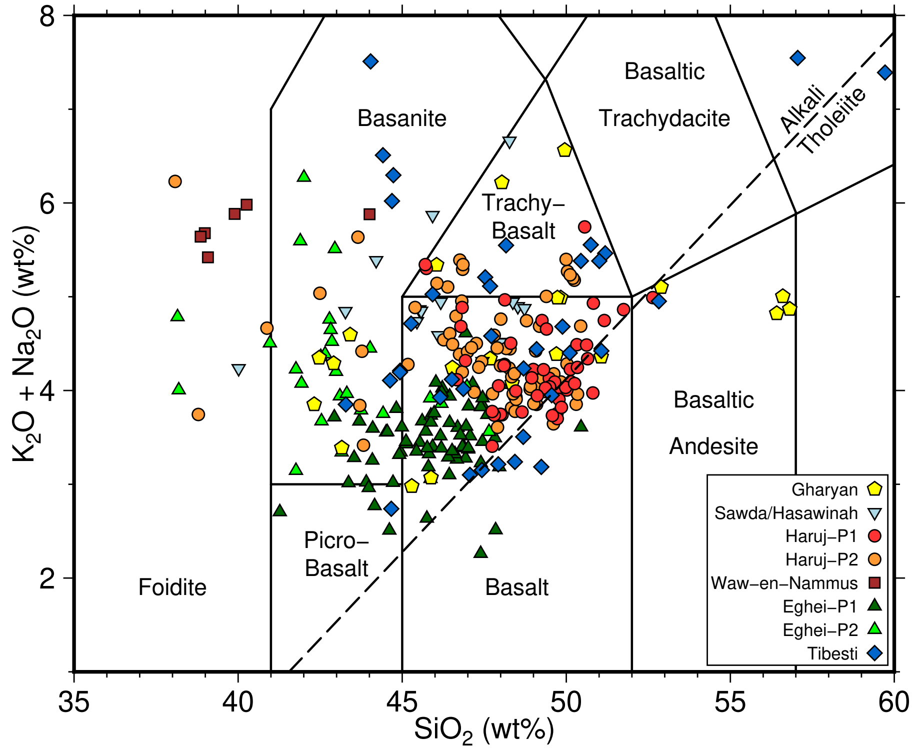

Figure 4. Total alkalis (i.e. $K_2O + Na_2O$) plotted as function of SiO_2 for volcanic samples whose locations are shown on Figure 2. Sub-division and nomenclature follows standard categorization scheme of *Le Maitre* [2002]. Dashed line = Alkali-Tholeiite divide redrawn from [*Irvine and Baragar*, 1971].

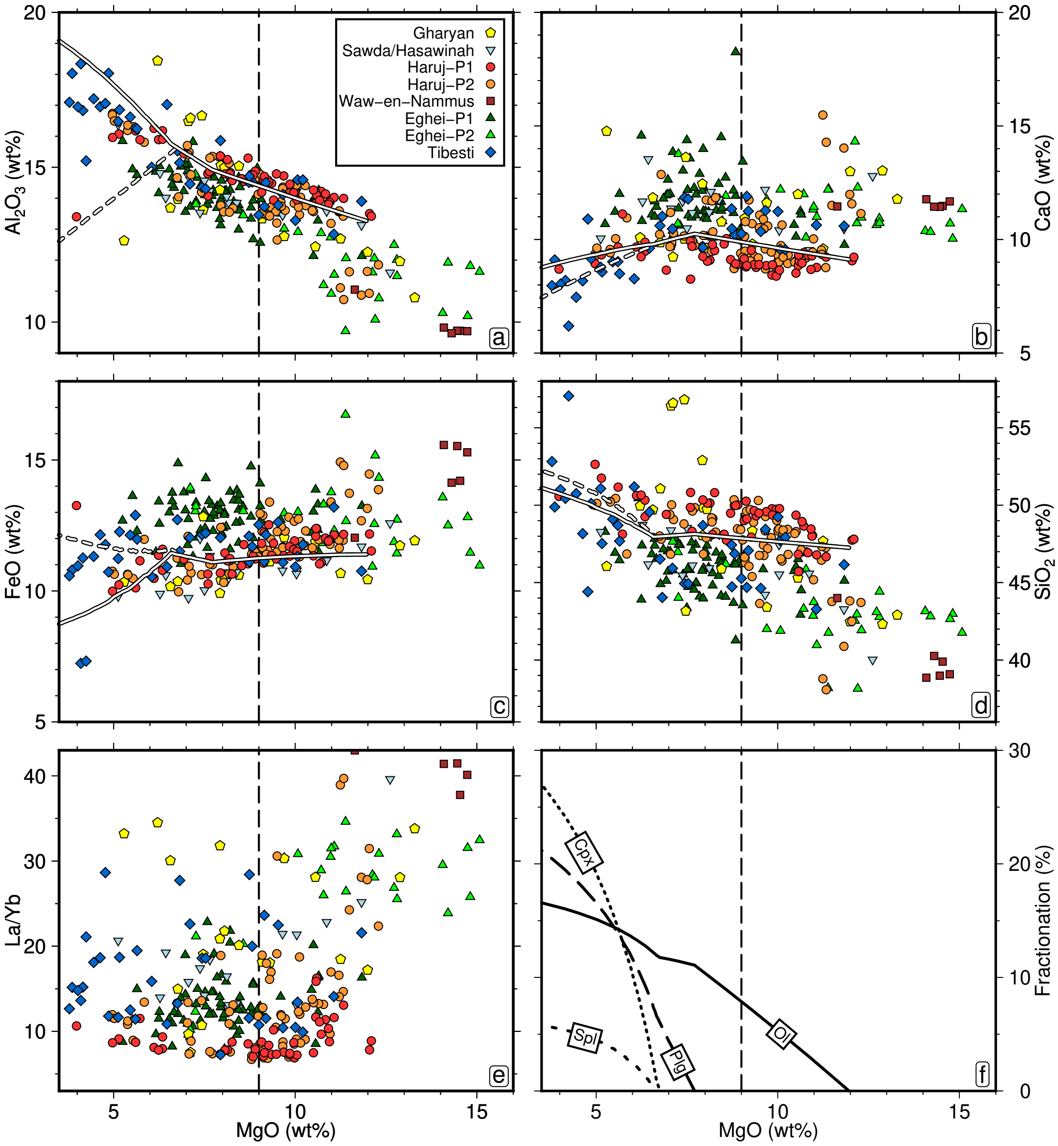

Figure 5. (a) Al_2O_3 plotted as function of MgO for volcanic samples whose locations are shown on Figure 2. Solid/dashed white lines = fractional crystallisation pathways that exclude/include plagioclase fractionation calculated for Sample 3.2 using Petrolog3 algorithm [*Danyushevsky and Plechov*, 2011]; vertical dashed line delineates 9 wt% value of MgO. (b)–(e) Same for CaO, FeO, SiO_2 and La/Yb as function of MgO. (f) Cumulative fractionation of each mineral used to generate dashed white lines in panels (a)–(e) where Ol = olivine, Cpx = clinopyroxene, Plg = plagioclase, Spl = spinel. Petrolog3 calculations assume olivine, clinopyroxene and spinel parametrizations of *Beattie* [1993], *Langmuir et al.* [1992] and *Nielsen* [1985], respectively; K_d for olivine= 0.3; pressure correction for spinel = 15 °C / kbar; value of $f(O_2)$ taken from *Kilinc et al.* [1983] with deviation of 2 log units; value of Fe_2O_3 for melt calculated using QFM $f(O_2)$ buffer.

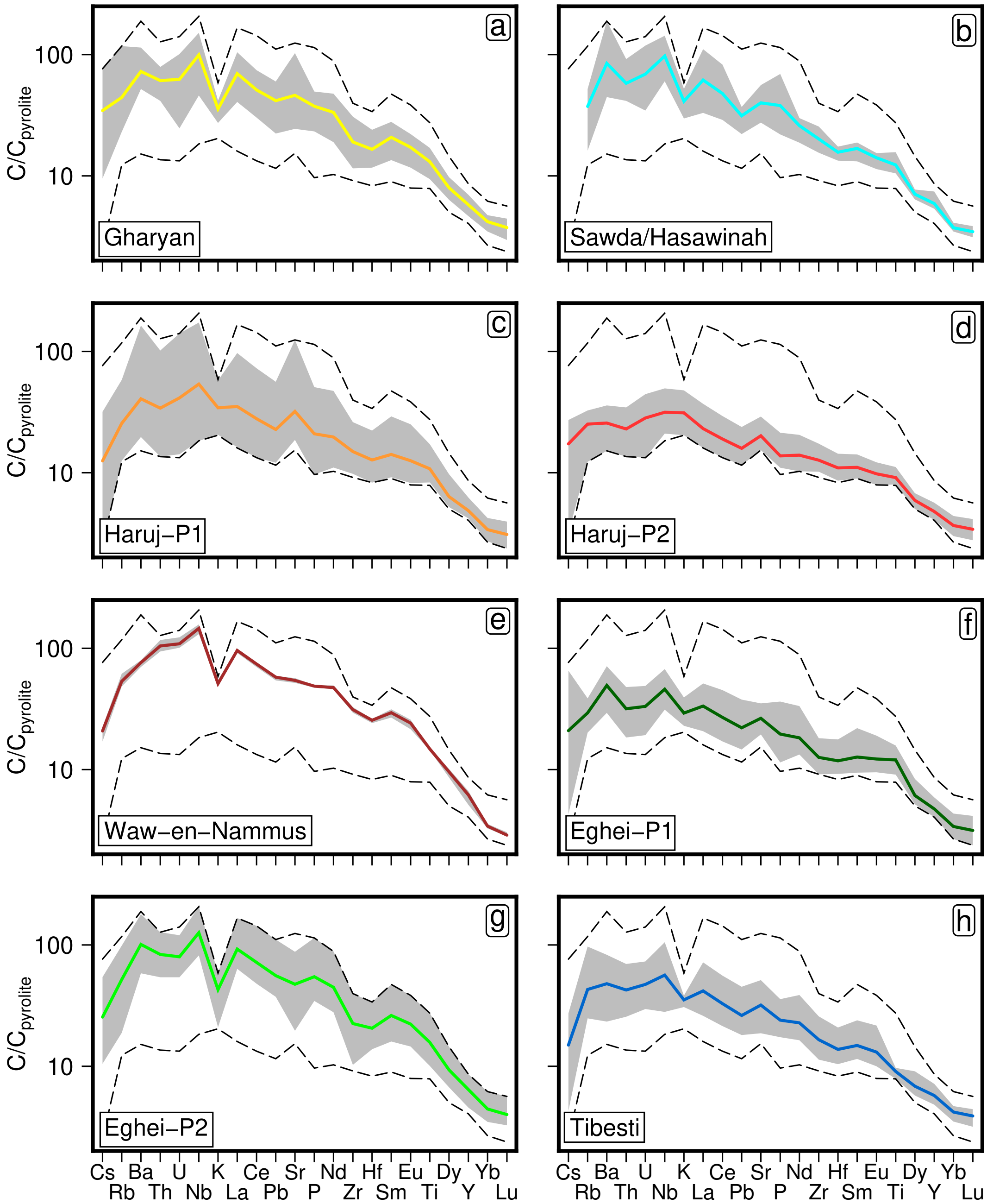

1301 **Figure 6.** (a) Trace element distribution of selected samples from Gharyan province chosen in accordance
1302 with criteria described in text. Compositions are normalized with respect to primitive mantle [*McDonough*
1303 *and Sun*, 1995]. Yellow line with gray band = mean value and range for province; pair of dashed lines = range
1304 of compositions from all provinces where MgO < 9 wt%. (b)–(h) Same for Sawda, Haruj-P1, Haruj-P2,
1305 Waw-en-Nammus, Eghei-P1, Eghei-P2 and Tibesti provinces.

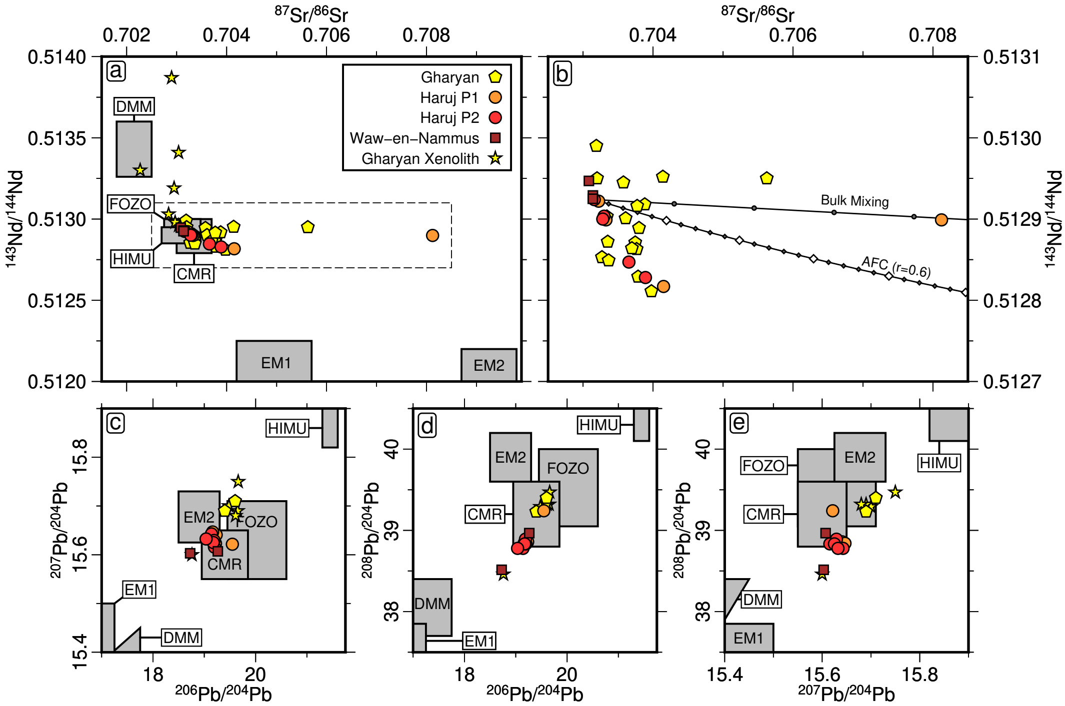

Figure 7. Isotopic compositions for selected samples from Libya and Chad. (a) $^{143}Nd/^{144}Nd$ ratios plotted as function of $^{87}Sr/^{86}Sr$. Circles are colored according to province, as indicated in panel at top right-hand side; labeled gray polygons = mantle reservoirs where DMM is depleted MORB mantle, FOZO is focal zone reservoir, HIMU is high-μ mantle, CMR is common mantle reservoir [*Lustrino and Wilson*, 2007], and EM1/EM2 is enriched mantle 1/2 [*Zindler and Hart*, 1986]; dashed box = locus of panel b. (b) Blow-up of panel a. Mixing lines between sample 4.10A from this study and granite sample TbM2 from *Suayah et al.* [2006]. Solid line with black circles = bulk mixing trend plotted at 1% intervals; solid line with black/open diamonds = assimilation and fractional crystallization (AFC) trend plotted at 1% and 5% intervals, respectively. (c) $^{207}Pb/^{204}Pb$ as function of $^{206}Pb/^{204}Pb$. (d) $^{208}Pb/^{204}Pb$ as function of $^{206}Pb/^{204}Pb$. (e) $^{208}Pb/^{204}Pb$ as function of $^{207}Pb/^{204}Pb$.

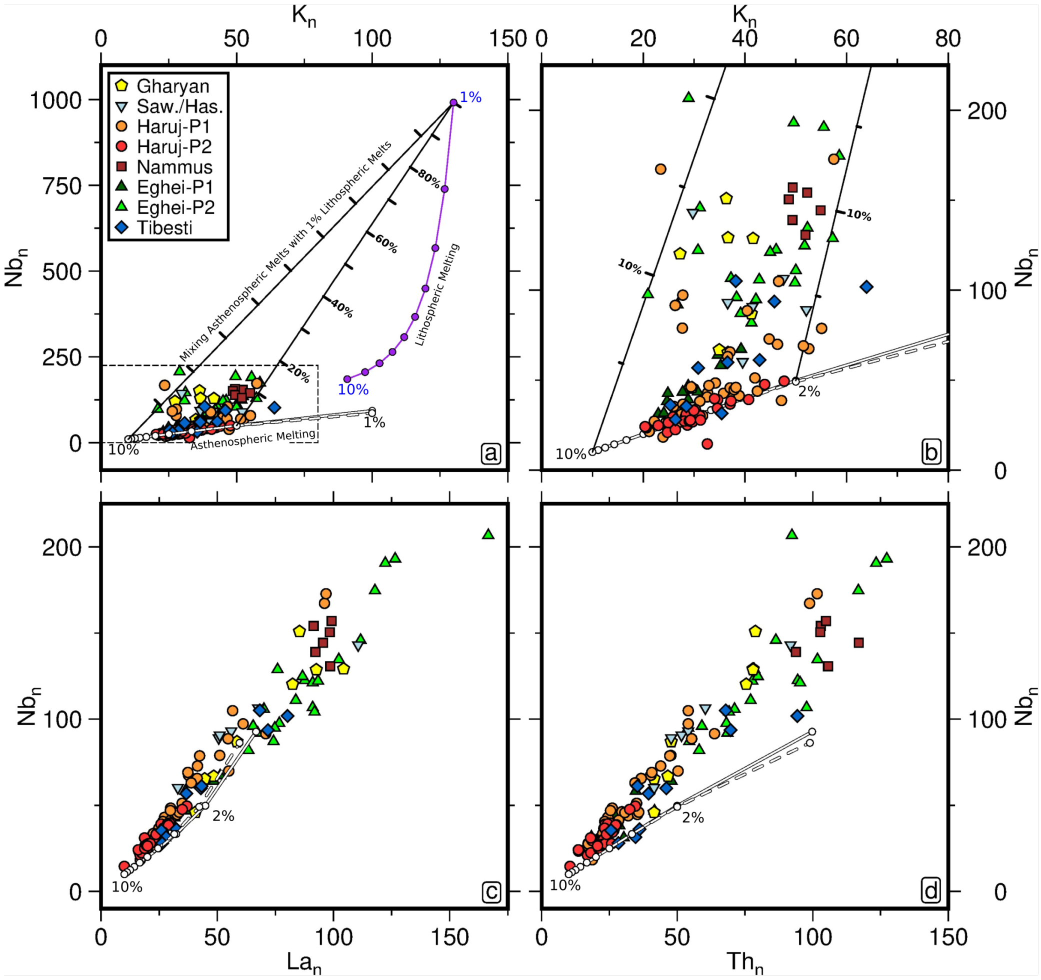

Figure 8. (a) Nb$_n$ plotted as function of K$_n$ for amphibole-bearing and amphibole-free lherzolites with MgO > 9 wt% where subscript n indicates that values are normalized with respect to primitive mantle. Solid/dashed white lines = trends for asthenospheric partial melting of primitive mantle at 15/30 kbar using mantle mineralogy and modal melting model of *Jennings and Holland* [2015], assuming source composition of *McDonough and Sun* [1995]; circles plotted every 1% of melting up to 10%; purple line = trend for lithospheric partial melting of primitive mantle using average source composition based upon analyses of mantle xenoliths from *Beccaluva et al.* [2008], modal mineralogy and modal melting model of *Späth et al.* [2001] with initial amphibole content of 5% using distribution coefficients from *Gibson and Geist* [2010]; circles plotted every 1% of melting up to 10%; pair of black lines with tick marks = mixing lines between 2% and 10% of asthenospheric melt and 1% of lithospheric melt; dashed box = locus of panel b. (b) Blow-up of panel a. (c) and (d) Nb$_n$ plotted as function of La$_n$ and as function of Th$_n$. Solid/dashed white lines as before.

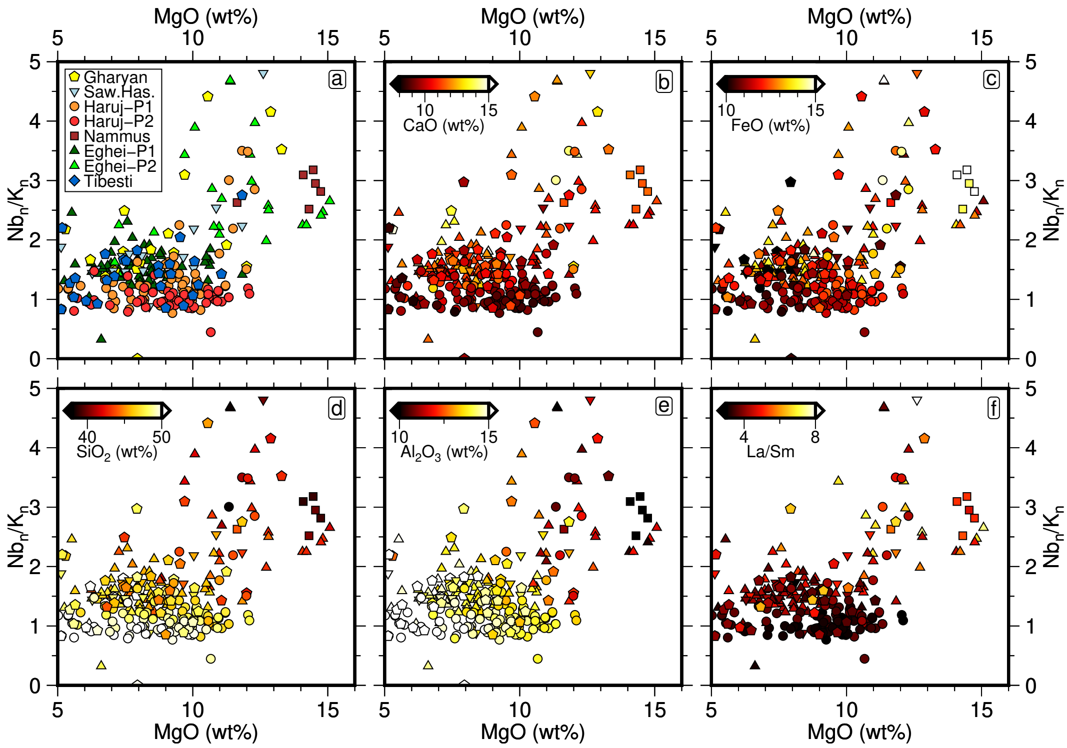

1327 **Figure 9.** (a) Nb_n/K_n plotted as function of MgO. Each symbol is colored according to geographic
1328 province, as indicated in panel at top right-hand side. (b)–(f) Same where each symbol is colored according to
1329 wt% of CaO, FeO, SiO_2, Al_2O_3 and La/Sm, respectively.

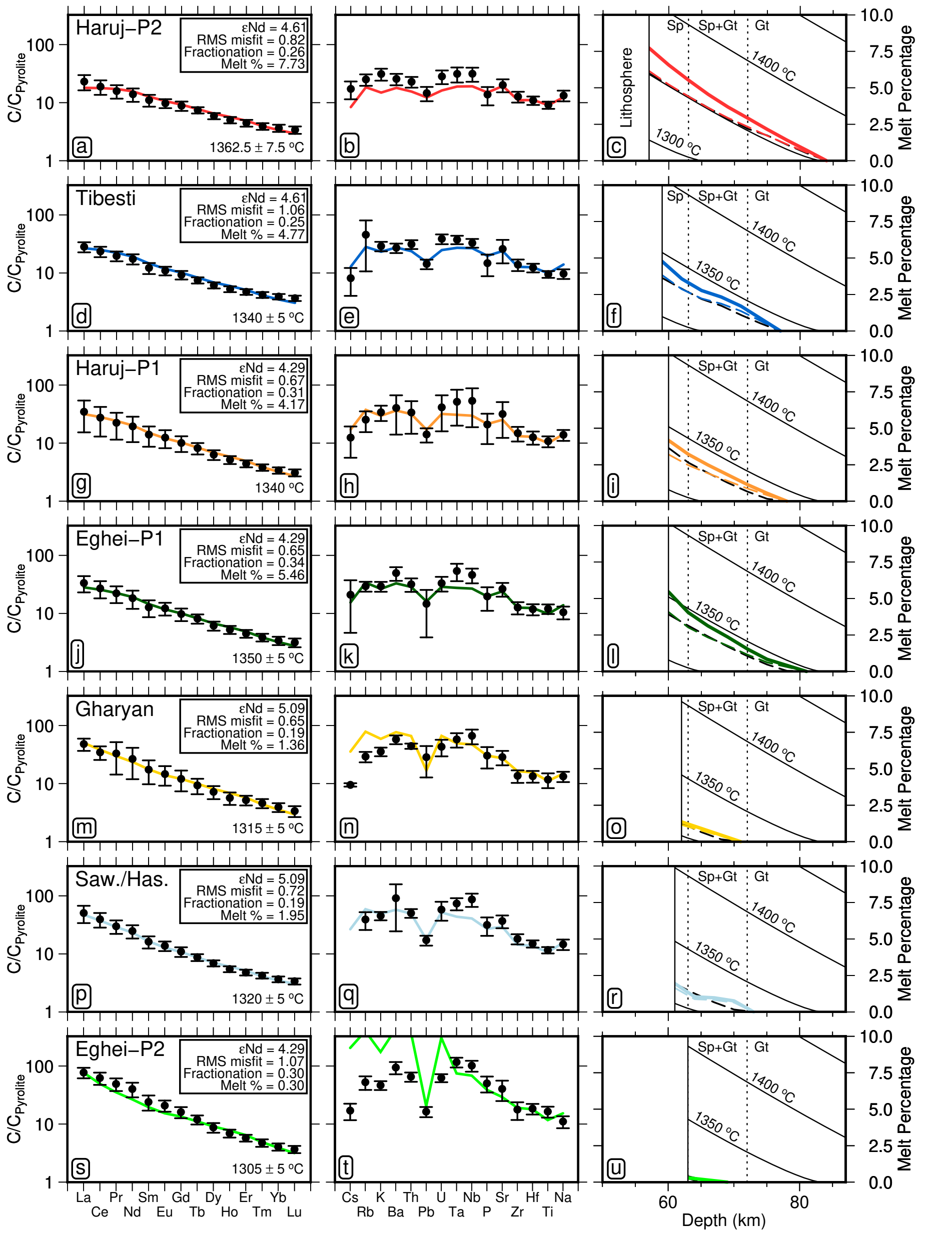

Figure 10. Inverse modeling of screened samples that have $>$ 9 wt% MgO [*McKenzie and O'Nions*, 1991]. (a) Rare earth element (REE) concentrations for samples from Haruj-P2 province normalized with respect to primitive mantle [*McDonough and Sun*, 1995]. Source composition calculated from ϵNd value, assuming mixture of Depleted MORB Mantle (DMM) and Primitive Mantle (PM). Black circles with vertical bars = average concentrations $\pm 1\sigma$; red line = best-fit concentrations calculated by inverse modeling. Inset panel summarizes: (i) ϵNd value; (ii) rms misfit value; (iii) fraction of added olivine; and (iv) cumulative melt percentage. (b) Trace element concentrations for Haruj-P2. Black circles with vertical bars = average concentrations $\pm 1\sigma$; red line = concentrations predicted by forward modeling. (c) Melt fraction as function of depth. Red line = melt fraction corrected for olivine fractionation obtained by fitting average REE concentrations shown in panel (a); red dashed line = same but uncorrected for olivine fractionation; black dashed line = starting distribution of melt fraction; solid black lines = isentropic curves calculated using parametrization of *Katz et al.* [2003] and labeled according to potential temperature; vertical dotted lines = phase transitions for spinel and garnet at 63 and 72 km; right-hand vertical line of gray bar = base of lithosphere used for inverse modeling. (d)–(f) Same for Tibesti. (g)–(i) Same for Haruj-P1. (j)–(l) Same for Eghei-P1. (m)–(o) Same for Eghei-P2. (p)–(r) Same for Sawda/Hasawinah. (s)–(u) Same for Gharyan.

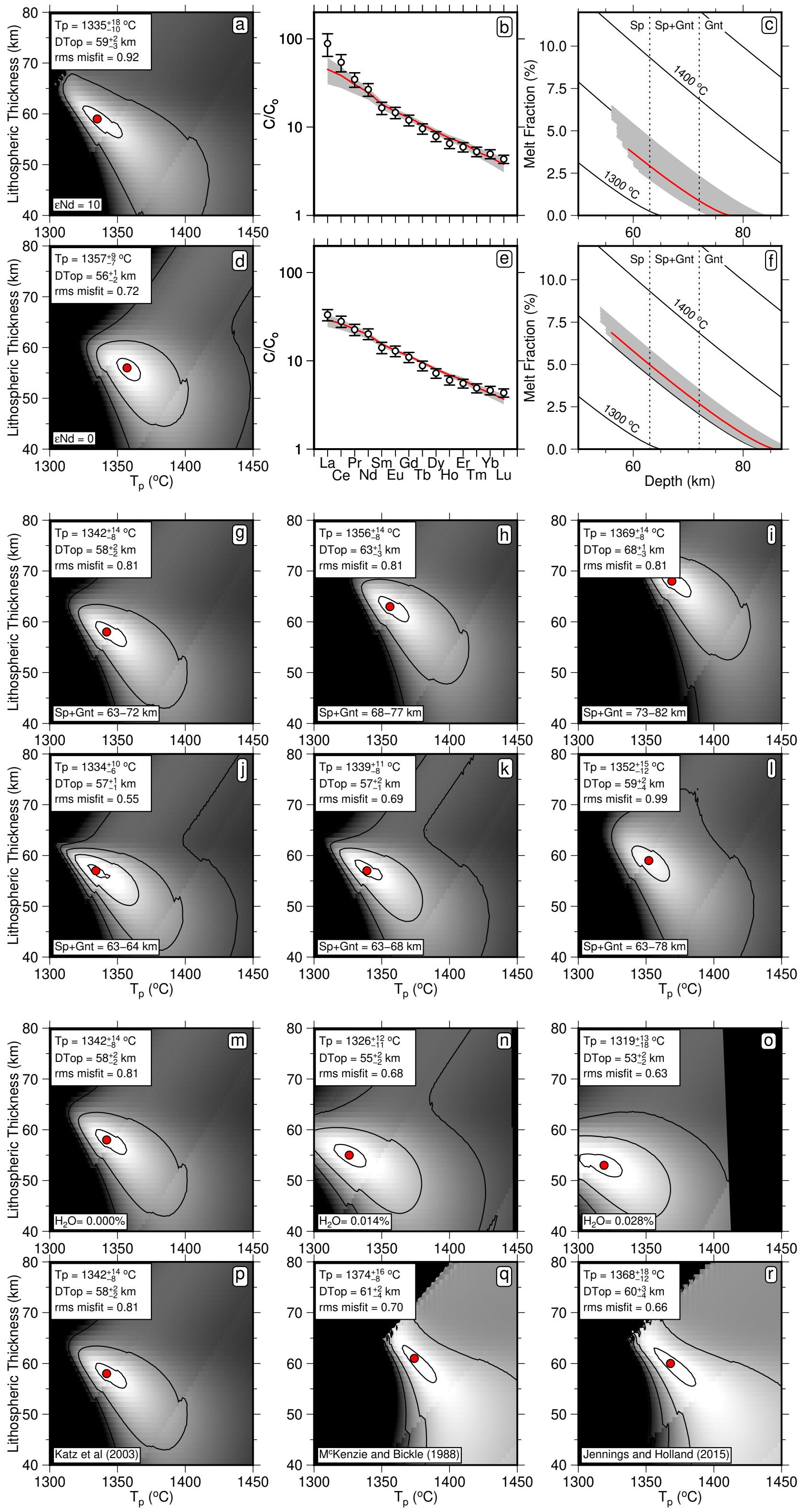

Figure 11. (a) Value of rms misfit between observed and calculated REE distribution for Tibesti province plotted as function of potential temperature, T_P, and lithospheric thickness, a, assuming depleted mantle source (i.e. εNd = 10). Contour lines plotted at intervals of 1.25 times misfit value at global minimum; red circle = global minimum; optimal values of T_P, a and rms misfit at global minimum shown in top left-hand corner. Pair of diagonal discontinuities evident in contour lines indicate loci where spinel or garnet enter/exit region of melting region. (b) Rare earth element (REE) concentrations for samples from Tibesti province normalized to source concentration. Black circles with vertical bars = average concentrations $\pm 1\sigma$; gray band = calculated concentrations within rms misfit = 1.25 of optimal model; red line = best-fit concentrations calculated by forward modeling assuming that melt fraction as function of depth follows adiabatic gradient. (c) Melt fraction as function of depth. Red line = adiabatic melting model obtained by fitting average REE concentrations shown in panel (a); gray band = results which fall within rms misfit = 1.25 of optimal model for different combinations of T_p-a pairs; solid black lines = isentropic curves calculated using parametrization of *Katz et al.* [2003] and labeled according to potential temperature; vertical dotted lines = phase transitions for spinel and garnet at 63 and 72 km. (d)–(f) Same for primitive mantle source (i.e. ϵNd = 0). Unless otherwise stated, each model assumes εNd = 4.61, spinel-garnet-transition zone = 63–72 km, and anhydrous melt model of *Katz et al.* [2003]. Starting melt fraction as function of depth is discretized every 1 km if melt path is < 25 km long, every 2 km if melt path is < 50 km long, and every 4 km if melt path is > 50 km long. (g)–(i) Residual misfit plots where depths to top and base of spinel-garnet transition are increased by increments of 5 km (i.e. 63–72 km; 68–77 km; 73–82 km). (j)–(l) Residual misfit plots where depth to base of spinel-garnet transition in increased by increments of 5 km (i.e. 63–64 km; 63–68 km; 63–78 km). (m)–(o) Residual misfit plots where water content of mantle source is varied (i.e. H_2O = 0.00 wt%; H_2O = 0.0014 wt%; H_2O = 0.028 wt%). (p)–(r) Residual misfit plots where three different mantle melting models are employed [*Katz et al.*, 2003; *McKenzie and Bickle*, 1988; *Jennings and Holland*, 2015].

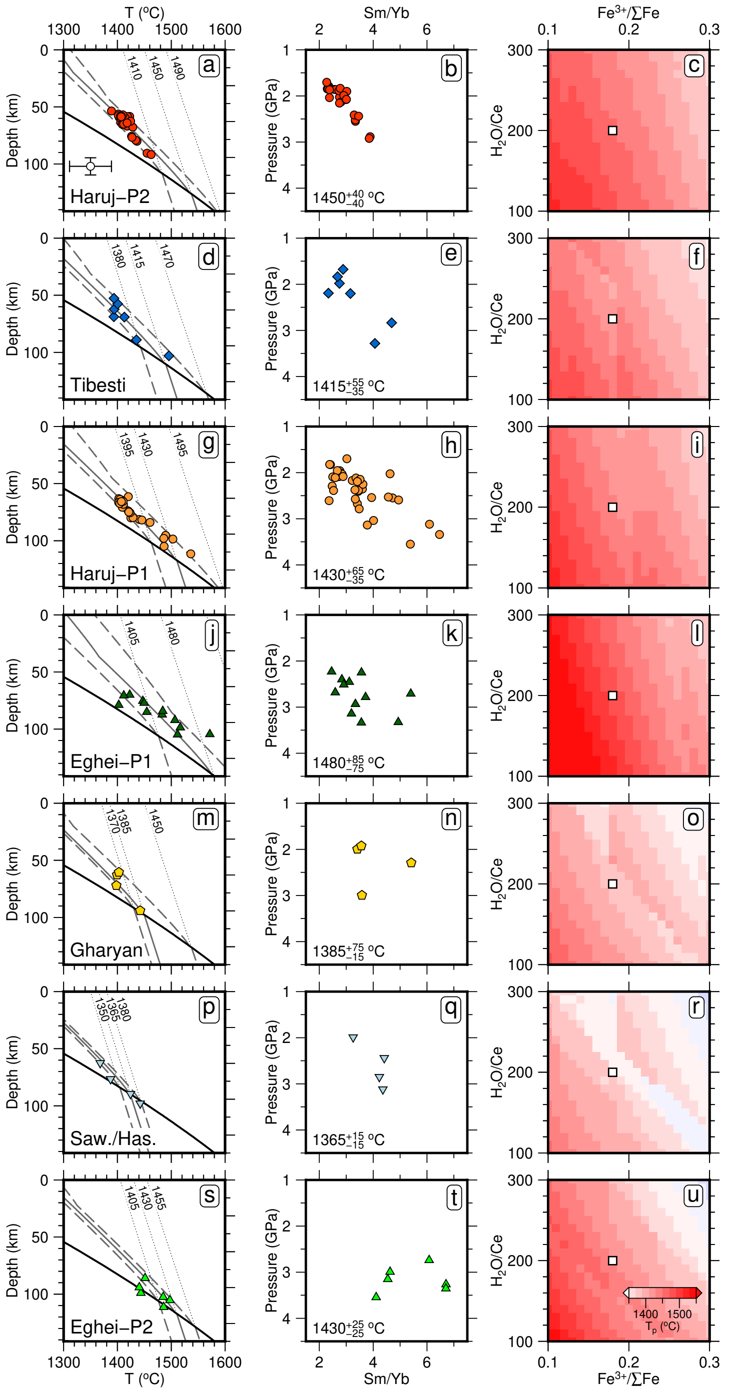

Figure 12. Thermobarometric calculations. (a) Temperature plotted as function of depth/pressure. Colored circles = equilibration pressure and temperature estimates determined for mafic samples from Haruj-P2 province using formulation of *Plank and Forsyth* [2016] where MgO> 9 wt%, $Nb_n/K_n < 2$, $Fe^{3+}/\Sigma Fe = 0.18$ and $H_2O/Ce = 200$. Black line = anhydrous solidus; gray line = best-fitting melt pathway where Mcpx = 0.15; dashed gray lines = minimum and maximum melt pathways for which misfit value at global minimum is double; dotted gray lines = adiabatic gradients corresponding to loci of intersections between melt pathways and anhydrous solidus [*Katz et al.*, 2003]; circle with cross in upper right-hand corner indicates uncertainties in temperature and pressure estimates; optimal value of potential temperature = 1450 ± 40 °C. (b) Sm/Yb ratios plotted as function of calculated pressures. (c) Contour map of calculated potential temperature as function of $Fe^{3+}/\Sigma Fe$ and H_2O/Ce. White circle = optimal value of potential temperature from panel a. (d)–(f) Tibesti. (g)–(i) Haruj-P1. (j)–(l) Eghei-P1. (m)–(o) Gharyan. (p)–(r) Sawda/Hasawinah. (s)–(u) Eghei-P2.

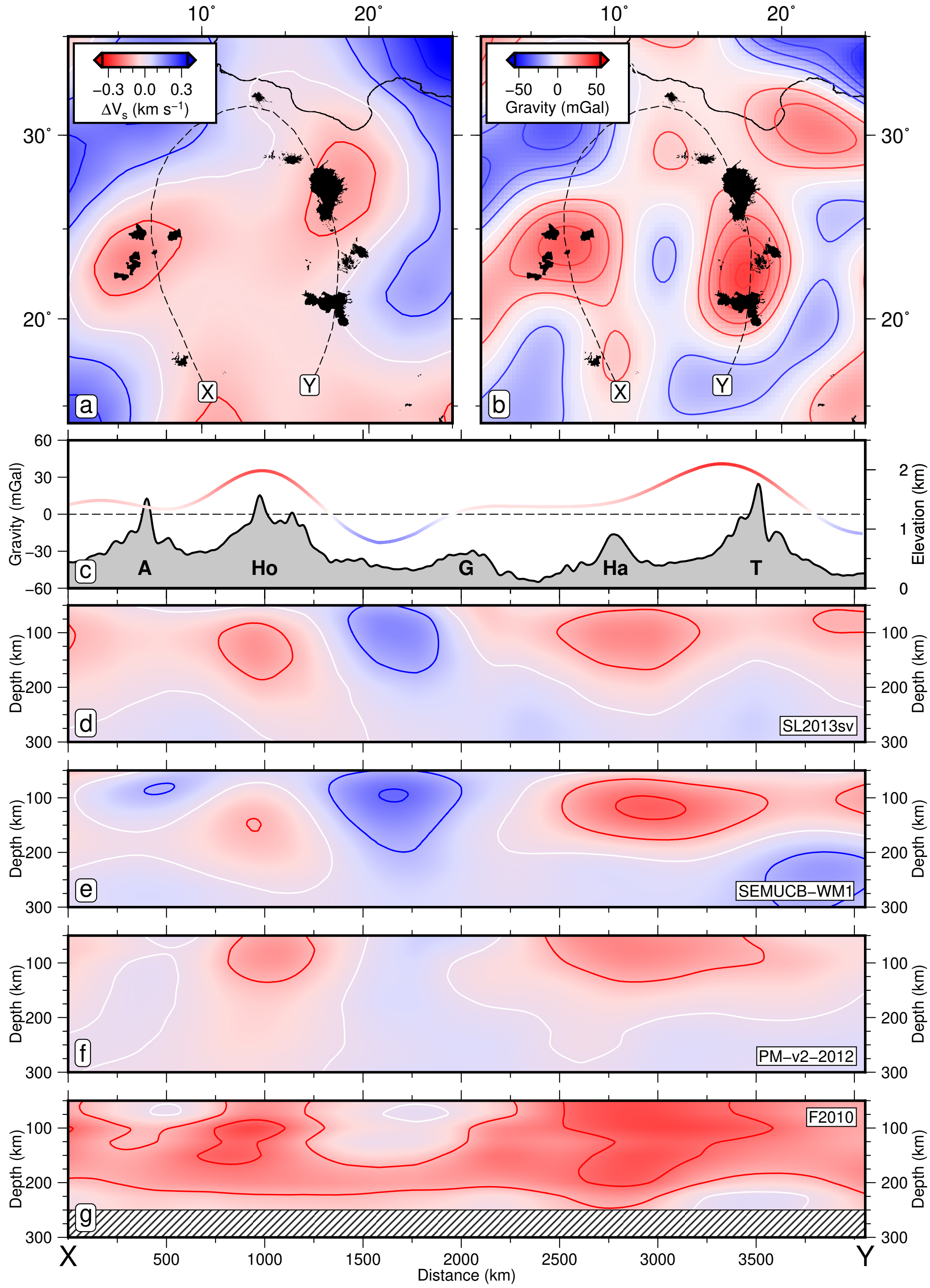

Figure 13. (a) Horizontal slice at 150 km depth through SL2013sv tomographic model [*Schaeffer and Lebedev*, 2013]. Blue/white/red contours = positive/zero/negative shear wave velocity anomalies plotted at 0.1 km s^{-1} intervals; black polygons = distribution of mafic volcanic rocks; dashed line labeled *X*–*Y* = location of transect shown in panels d–g. (b) Long wavelength (i.e. > 800 km) free-air gravity anomalies calculated from DIR-R5 database [*Bruinsma et al.*, 2014]. Red/white/blue contours = positive/zero/negative gravity anomalies plotted at 10 mGal intervals. (c) Topographic and gravity transects. Black line with gray band = topographic profile; red/blue line = long wavelength free-air gravity anomalies; horizontal dashed line = zero value; A = Aïr, Ho = Hoggar, H = Haruj and T = Tibesti swells. (d)–(g) Vertical slices through SL2013sv, SEMUCB-WM1, PM-2012-v2, and F2010 tomographic models. Hatched box delimits vertical extent of F2010 model. Color scheme for all tomographic models same as Figure 13a.

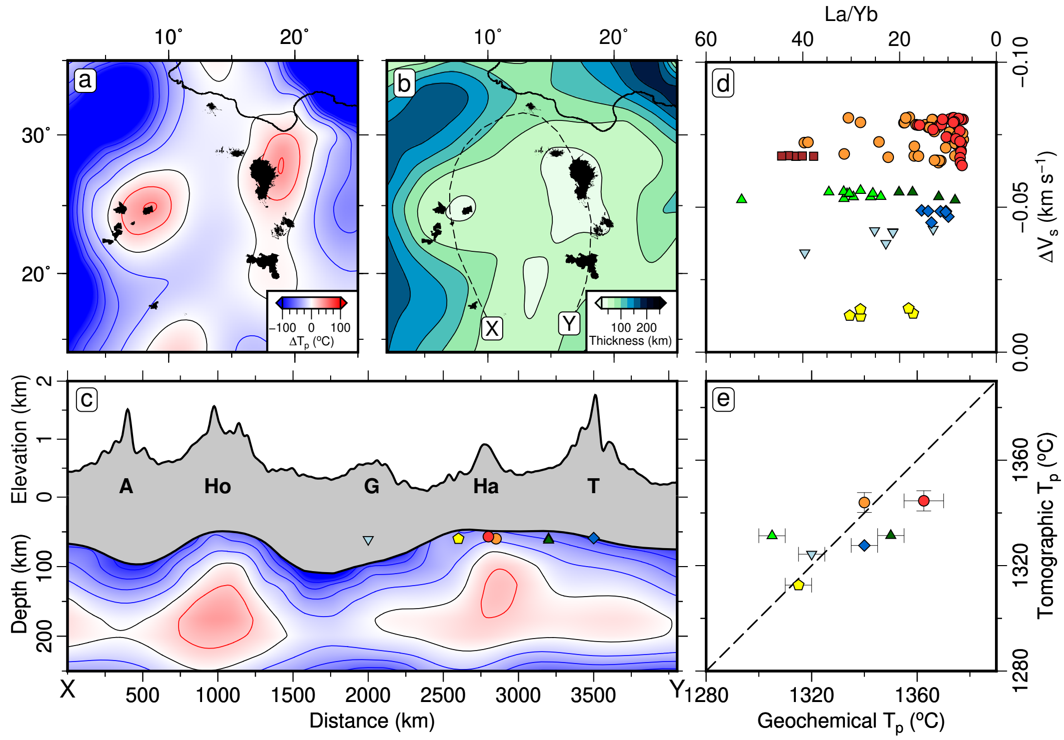

Figure 14. (a) Horizontal slice at depth of 150 km showing calculated potential temperature, T$_P$, estimated from PM – 2012 – v2 tomographic model using V_S-T parameterization of *Yamauchi and Takei* [2016]. Temperature is converted into T$_P$ assuming adiabatic gradient of 0.6°C/km with ambient mantle of T$_P$ = 1330°C. Red/black/blue contours = potential temperature values plotted at intervals of 20 °C; black polygons = distribution of mafic volcanic rocks. (b) Calculated lithospheric thickness determined from intersection of constructed temperature profiles with 1300 °C isotherm. Dashed line labeled *X–Y* = location of transect shown in panel c. (c) Vertical slice through calculated temperature structure. Black line with gray band = topographic profile; A = Aïr, Ho = Hoggar, H = Haruj and T = Tibesti swells; colored symbols = tops of melting column for each volcanic area determined by inverse modeling using INVMEL algorithm (yellow pentagons = Gharyan; turquoise inverted triangles = Sawda and Hasawinah; red/orange circles = Haruj P2/P1; maroon squares = Waw-en-Nammus; dark green/light green triangles = Jabal Eghei P2/P1; blue diamonds = Tibesti). (d) Average shear wave velocity, V_s for depth range of 100–200 km plotted as function of La/Sm ratio for 113 individual samples with MgO > 9 wt% (see Figure 2 for locations). (e) Potential temperature calculated from average V_s anomalies for depth range of 100–200 km plotted as function of potential temperature calculated from inverse modeling of rare earth element distributions. Dotted line = 1:1 relationship for visual guidance. Colored symbols with error bars as in panel d.

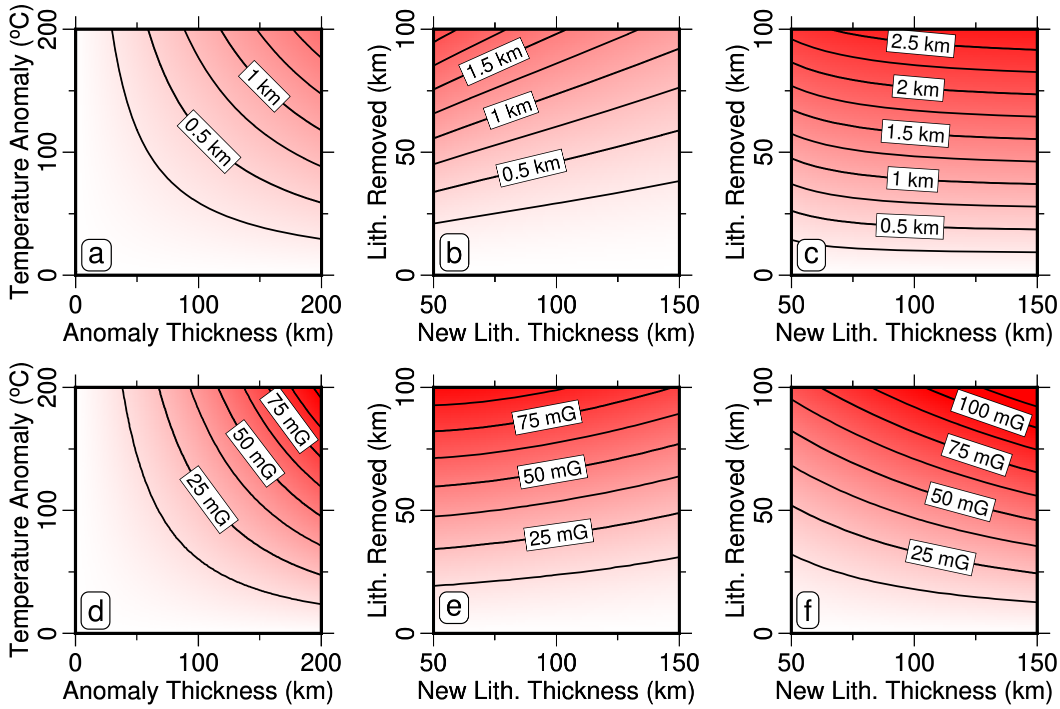

Figure 15. (a) Uplift calculated as function of thickness of asthenospheric layer beneath plate and its temperature anomaly. (b) Uplift calculated as function of present-day lithospheric thickness and removed lithospheric thickness. (c) Same but assuming that present-day lithosphere has re-equilibrated. (d)–(f) Calculated free-air gravity anomalies for asthenospheric channel and for disequilibrated/requilibrated lithosphere, respectively. See text for further details.

Acknowledgments

PB acknowledges support by Shell Research. MJH acknowledges support by National Aeronautics and Space Administration grant NNX17AE17G. CO is supported by Natural Environment Research Council centre for the observation and modelling of earthquakes, volcanoes and tectonics. SK is supported by Deutsche ForschungsGemeinschaft project number 57444011-SFB806. NJW and SN thank G. Roberts, M. Shann, B. Grenat, H.M. Emhmef, K.M. Lehemaf, A. Abdallha, N. Hussoin, A., Abddallha and A. Alsnosey for their unstinting help and enthusiasm in the Libyan desert. We are grateful to J. Day, I. Frame, L. Kennan, M. Klöcking, D. Lyness, S. Matthews, F. McNab, N. Odling, F. Richards, O. Shorttle, S. Stephenson and K. Warners for their help. D. McKenzie generously provided software for calculating admittance and INVMEL. D. Schutt, M. Wilson and J. C. Afonso wrote careful and insightful reviews. Geochemical and other databases are either publicly available or listed in Supplementary Information and available in the University of Cambridge online repository, doi.org/10.17863/CAM.40525. The INVMEL software package is available on request from D. McKenzie. Figures were prepared using Generic Mapping Tools software [*Wessel and Smith*, 1991]. Department of Earth Sciences contribution number esc.4481.

References

Abadi, A. M., J.-D. van Wees, P. M. van Dijk, and S. A. Cloetingh (2008), Tectonics and subsidence evolution of the Sirt Basin, Libya, *AAPG bulletin*, *92*(8), 993–1027.

Abdunaser, K. M., and K. J. McCaffrey (2015), Tectonic history and structural development of the Zallah-Dur al Abd Sub-basin, western Sirt Basin, Libya, *Journal of Structural Geology*, *73*, 33–48, doi:10.1016/j.jsg.2015.02.006.

Abdunaser, K. M., K. J. W. McCaffrey, E. A. Al-heety, D. P. Heron, G. Meinhold, M. Elgadry, Y. Abutarruma, and D. Boote (2014), Rift architecture and evolution: The Sirt Basin, Libya: The influence of basement fabrics and oblique tectonics, *Journal of African Earth Sciences*, *100*, 203–226, doi:10.1016/j.jafrearsci.2014.06.020.

Ade-Hall, J. M., S. Gerstein, R. E. Gerstein, P. H. Reynolds, P. Dagley, A. E. Mussett, and T. P. Hubbard (1975a), Geophysical Studies of North African Cenozoic Volcanic Areas: III. Garian, Libya, *Canadian Journal of Earth Sciences*, *12*, 1264–1271.

Ade-Hall, J. M., P. H. Reynolds, P. Dagley, A. E. Mussett, and T. P. Hubbard (1975b), Geophysical Studies of North African Cenozoic Volcanic Areas: II. Jebel Soda, Libya, *Canadian Journal of Earth Sciences*, *12*(8), 1257–1263.

Anderson, D. L. (2005), Scoring hotspots: The plume and plate paradigms, *Special Papers - Geological Society of America*, *388*, 31.

Audet, P. (2014), Toward mapping the effective elastic thickness of planetary lithospheres from a spherical wavelet analysis of gravity and topography, *Physics of the Earth and Planetary Interiors*, *226*, 48–82, doi:10.1016/j.pepi.2013.09.011.

Bardintzeff, J.-M., C. Deniel, H. Guillou, B. Platevoet, P. Telouk, and K. M. Oun (2012), Miocene to recent alkaline volcanism between Al Haruj and Waw an Namous (southern Libya), *International Journal of Earth Sciences*, *101*(4), 1047–1063, doi:10.1007/s00531-011-0708-5.

Bassin, C., G. Laske, and G. Masters (2000), The current limits of resolution for surface wave tomography in North America, *EOS Trans AGU*, *81*(F897).

Beattie, P. (1993), Olivine-melt and orthopyroxene-melt equilibria, *Contributions to Mineralogy and Petrology*, *115*(1), 103–111.

Beccaluva, L., G. Bianchini, R. M. Ellam, M. Marzola, K. M. Oun, F. Siena, and F. M. Stuart (2008), The role of HIMU metasomatic components in the North African lithospheric mantle: petrological evidence from the Gharyan lherzolite xenoliths, NW Libya, *Geological Society, London, Special Publications*, *293*(1), 253–277, doi:10.1144/SP293.12.

Becker, J. J., D. T. Sandwell, W. H. Smith, J. Braud, B. Binder, J. Depner, D. Fabre, J. Factor, S. Ingalls, S. H. Kim, R. Ladner, K. Marks, S. Nelson, A. Pharaoh, R. Trimmer, J. von Rosenberg, G. Wallace, and P. Weatherall (2009), Global Bathymetry and Elevation Data at 30 Arc Seconds Resolution: SRTM30_PLUS, *Marine Geodesy*, *32*(4), 355–371, doi:10.1080/01490410903297766.

Bergman, S. C., K. A. Foland, and F. J. Spera (1981), On the origin of an amphibole-rich vein in a peridotite inclusion from the Lunar Crater Volcanic Field, Nevada, U.S.A., *Earth and Planetary Science Letters*, *56*, 343–361.

Blundy, J., and B. Wood (2003), Partitioning of trace elements between crystals and melts, *Earth and Planetary Science Letters*, *210*(3-4), 383–397, doi:10.1016/S0012-821X(03)00129-8.

Bosworth, W. (2008), North Africa–Mediterranean present-day stress field transition and implications for fractured reservoir production in the eastern Libyan basins, *Geology of East Libya*, *4*(1992), 123–138.

Brounce, M., K. Kelley, and E. Cottrell (2014), Variations in Fe3+/$\sum$Fe of Mariana Arc Basalts and Mantle Wedge fO_2, *Journal of Petrology*, *55*(12), 2513–2536.

Bruinsma, S. L., C. Förste, O. Abrikosov, J.-C. Marty, M.-H. Rio, S. Mulet, and S. Bonvalot (2013), The new ESA satellite-only gravity field model via the direct approach, *Geophysical Research Letters*, *40*(14), 3607–3612, doi:10.1002/grl.50716.

Bruinsma, S. L., C. Förste, O. Abrikosov, J.-M. Lemoine, J.-C. Marty, S. Mulet, M.-H. Rio, and S. Bonvalot (2014), ESA's satellite-only gravity field model via the direct approach based on all GOCE data, *Geophysical Research Letters*, *41*(21), 7508–7514.

Burke, K. (1996), The African Plate, *South african journal of geology*, *99*(4), 341–409.

Burke, K., and Y. Gunnell (2008), The African Erosion Surface: A Continental-Scale Synthesis of Geomorphology, Tectonics, and Environmental Change over the Past 180 Million Years, *GSA Memoirs*, *20-1*, 1–66.

Busrewil, M. T., and J. Esson (1991), Chronology and Composition of the Igneous Rocks of Jabal as Sawda, in *The Geology of Libya*, edited by M. J. Salem, M. T. Busrewil, and A. M. Ben Ashour, pp. 2599–2603, Elsevier B.V, Amsterdam.

Busrewil, M. T., and K. M. Oun (1991), Geochemistry of the Tertiary Alkaline Rocks of Jabal al Hasawinah, West Central Libya, in *The Geology of Libya*, edited by M. J. Salem, M. T. Busrewil, and A. M. Ben Ashour, pp. 2587–2598, Elsevier B.V., Amsterdam.

Busrewil, M. T., and W. J. Wadsworth (1982), The basalts and associated lherzolite xenoliths of Waw-an-Namus Volcano, Libya, *Libyan Journal of Science*, *2*, 19–28.

Colli, L., H. P. Bunge, and B. S. Schuberth (2015), On retrodictions of global mantle flow with assimilated surface velocities, *Geophysical Research Letters*, *42*(20), 8341–8348, doi:10.1002/2015GL066001.

Conant, L. C., and G. H. Goudarzi (1964), Geologic map of the Kingdom of Libya, U.S. Geological Survey Miscellaneous Geological Investigations Map 1-350-A, scale 1:2000000, *Tech. rep.*

Conant, L. C., and G. H. Goudarzi (1967), Stratigraphic and tectonic framework of Libya, *AAPG bulletin*, *51*(5), 719–730.

Cottrell, E., K. A. Kelley, A. Lanzirotti, and R. A. Fischer (2009), High-precision determination of iron oxidation state in silicate glasses using XANES, *Chemical Geology*, *268*(3-4), 167–179, doi:10.1016/j.chemgeo.2009.08.008.

Courtillot, V., A. Davaille, J. Besse, and J. Stock (2003), Three distinct types of hotspots in the Earth's mantle, *Earth and Planetary Science Letters*, *205*(3-4), 295–308.

Cox, K. G. (1989), The role of mantle plumes in the development of continental drainage patterns, *Nature*, *342*, 873–876.

Cox, K. G. (1993), Continental magmatic underplating, *Phil. Trans. R. Soc. Lond. A*, *342*(1663), 155–166.

Crosby, A., and D. McKenzie (2009), An analysis of young ocean depth, gravity and global residual topography, *Geophysical Journal International*, *178*(3), 1198–1219.

Crosby, A. G. (2007), An assessment of the accuracy of admittance and coherence estimates using synthetic data, *Geophysical Journal International*, *171*(1), 25–54, doi:10.1111/j.1365-246X.2007.03520.x.

Cvetković, V., M. Toljić, N. a. Ammar, L. Rundić, and K. B. Trish (2010), Petrogenesis of the eastern part of the Al Haruj basalts (Libya), *Journal of African Earth Sciences*, *58*(1), 37–50, doi:10.1016/j.jafrearsci.2010.01.006.

Dalton, C. A., C. H. Langmuir, and A. Gale (2014), Geophysical and geochemical evidence for deep temperature variations beneath mid-ocean ridges, *Science*, *344*(6179), 80–83.

Danyushevsky, L. V., and P. Plechov (2011), Petrolog3: Integrated software for modeling crystallization processes, *Geochemistry, Geophysics, Geosystems*, *12*(7).

Dasgupta, R., M. G. Jackson, and C. T. A. Lee (2010), Major element chemistry of ocean island basalts - Conditions of mantle melting and heterogeneity of mantle source, *Earth and Planetary Science Letters*, *289*(3-4), 377–392, doi:10.1016/j.epsl.2009.11.027.

Davies, G. F. (1988), Ocean bathymetry and mantle convection: 1. Large-scale flow and hotspots, *Journal of Geophysical Research: Solid Earth*, *93*(B9), 10,467–10,480.

Davis, F. A., and M. M. Hirschmann (2013), The effects of K_2O on the compositions of near-solidus melts of garnet peridotite at 3 GPa and the origin of basalts from enriched mantle, *Contributions to Mineralogy and Petrology*, *166*(4), 1029–1046.

Deniel, C., P. M. Vincent, A. Beauvilain, and A. Gourgaud (2015), The Cenozoic volcanic province of Tibesti (Sahara of Chad): major units, chronology, and structural features, *Bulletin of Volcanology*, *77*(9), 74, doi:10.1007/s00445-015-0955-6.

DePaolo, D. J. (1981), Trace element and isotopic effects of combined wallrock assimilation and fractional crystallization, *Earth and planetary science letters*, *53*(2), 189–202.

Dixon, J. E., L. Leist, C. Langmuir, and J.-G. Schilling (2002), Recycled dehydrated lithosphere observed in plume-influenced mid-ocean-ridge basalt., *Nature*, *420*(6914), 385–389, doi:10.1038/nature01215.

Eggins, S., J. Woodhead, L. Kinsley, G. Mortimer, P. Sylvester, M. McCulloch, J. Hergt, and M. Handler (1997), A simple method for the precise determination ofâĽě 40 trace elements in geological samples by icpms using enriched isotope internal standardisation, *Chemical Geology*, *134*(4), 311–326.

Elshaafi, A., and A. Gudmundsson (2016), Volcano-tectonics of the Al Haruj Volcanic Province, Central Libya, *Journal of Volcanology and Geothermal Research*, *325*, 189–202, doi:10.1016/j.jvolgeores.2016.06.025.

Faul, U. H., and I. Jackson (2007), Diffusion creep of dry, melt-free olivine, *Journal of Geophysical Research*, *112*, 1–14.

Fishwick, S. (2010), Surface wave tomography: Imaging of the lithosphere-asthenosphere boundary beneath central and southern Africa?, *Lithos*, *120*(1-2), 63–73, doi:10.1016/j.lithos.2010.05.011.

Fitton, J., A. Saunders, L. Larsen, B. Hardarson, and M. Norry (1998), Volcanic rocks from the southeast Greenland margin at 63°N: composition, petrogenesis and mantle sources, *Proceedings of the Ocean Drilling Program, Scientific Results*, *152*, 197–208.

French, S. W., and B. A. Romanowicz (2014), Whole-mantle radially anisotropic shear velocity structure from spectral-element waveform tomography, *Geophysical Journal International*, *199*(3), 1303–1327, doi:10.1093/gji/ggu334.

Galer, S. J. G., and W. Abouchami (1998), Practical application of lead triple spiking for correction of instrumental mass discimination, *Mineralogy Magazine*, *62A*, 491–492.

Gautheron, C., and M. Moreira (2002), Helium signature of the subcontinental lithospheric mantle, *Earth and Planetary Science Letters*, *199*(1-2), 39–47, doi:10.1016/S0012-821X(02)00563-0.

Gibson, S. A., and D. Geist (2010), Geochemical and geophysical estimates of lithospheric thickness variation beneath Galápagos, *Earth and Planetary Science Letters*, *300*(3-4), 275–286, doi:10.1016/j.epsl.2010.10.002.

Gourgaud, A., and P. M. Vincent (2004), Petrology of two continental alkaline intraplate series at Emi Koussi volcano, Tibesti, Chad, *Journal of Volcanology and Geothermal Research*, *129*(4), 261–290, doi:10.1016/S0377-0273(03)00277-4.

Graham, D. W. (2002), Noble Gas Isotope Geochemistry of Mid-Ocean Ridge and Ocean Island Basalts: Characterization of Mantle Source Reservoirs, *Reviews in Mineralogy and Geochemistry*, *47*(1), 247–317, doi:10.2138/rmg.2002.47.8.

Green, E. C. R., T. J. B. Holland, R. Powell, and R. W. White (2012), Garnet and spinel lherzolite assemblages in MgO-Al_2O_3-SiO_2 and CaO-MgO-Al_2O_3-SiO_2: Thermodynamic models and an experimental conflict, *Journal of Metamorphic Geology*, *30*(6), 561–577, doi:10.1111/j.1525-1314.2012.00981.x.

Gumati, Y., and S. Schamel (1988), Thermal maturation history of the Sirte Basin, Libya, *Journal of Petroleum Geology*, *11*(2), 205–218.

Gunn, R. (1943), A quantitative evaluation of the influence of the lithosphere on the anomalies of gravity, *John Franklin Institute*, *236*, 373–396.

Hager, B., and M. Richards (1989), Long-wavelength variations in earthâĂŹs geoid: physical models and dynamical implications, *Philosophical Transactions of the Royal Society of London. Series A, Mathematical and Physical Sciences*, *328*(1599), 309–327.

Halldõrsson, S. A., D. R. Hilton, P. Scarsi, T. Abebe, and J. Hopp (2014), A common mantle plume source beneath the entire East African Rift System revealed by coupled helium-neon systematics, *Geophysical Research Letters*, *41*(7), 2304–2311, doi:10.1002/2014GL059424.

Hassan, H. S., and C. C. G. Kendall (2014), *Hydrocarbon Provinces of Libya: A Petroleum System Study*, American Association of Petroleum Geologists.

Herzberg, C., P. D. Asimow, N. Arndt, Y. Niu, C. Lesher, J. Fitton, M. Cheadle, and A. Saunders (2007), Temperatures in ambient mantle and plumes: Constraints from basalts, picrites, and komatiites, *Geochemistry, Geophysics, Geosystems*, *8*(2).

Irvine, T. N., and W. R. A. Baragar (1971), A Guide to the Chemical Classification of the Common Volcanic Rocks, *Canadian Journal of Earth Sciences*, *8*, 523–548.

Jennings, E. S., and T. J. B. Holland (2015), A simple thermodynamic model for melting of peridotite in the system NCFMASOCr, *Journal of Petrology*, *56*(5), 869–892, doi:10.1093/petrology/egv020.

Jochum, K. P., and U. Nohl (2008), Reference materials in geochemistry and environmental research and the GeoReM database, *Chemical Geology*, *253*, 50–53.

Jurák, L. (1978), *Geological Map of Libya; 1:250,000. Sheet: Jabal al Hasawinah NH*, 87 pp., Industrial Research Centre, Tripoli.

Katz, R. F., M. Spiegelman, and C. H. Langmuir (2003), A new parameterization of hydrous mantle melting, *Geochemistry, Geophysics, Geosystems*, *4*(9), doi:10.1029/2002GC000433.

Keshav, S., G. H. Gudfinnsson, G. Sen, and Y. Fei (2004), High-pressure melting experiments on garnet clinopyroxenite and the alkalic to tholeiitic transition in ocean-island basalts, *Earth and Planetary Science Letters*, *223*(3-4), 365–379.

Kilinc, A., I. Carmichael, M. L. Rivers, and R. O. Sack (1983), The ferric-ferrous ratio of natural silicate liquids equilibrated in air, *Contributions to Mineralogy and Petrology*, *83*(1-2), 136–140.

Klein, E. M., and C. H. Langmuir (1987), Global correlations of ocean ridge basalt chemistry with axial depth and crustal thickness, *Journal of Geophysical Research: Solid Earth*, *92*(B8), 8089–8115.

Klemme, S. (2004), The influence of Cr on the garnet-spinel transition in the Earth's mantle: Experiments in the system MgO-Cr_2O_3-SiO_2 and thermodynamic modelling, *Lithos*, *77*(1-4 SPEC. ISS.), 639–646, doi:10.1016/j.lithos.2004.03.017.

Klemme, S., and H. S. C. O'Neill (2000), The near-solidus transition from garnet lherzolite to spinel lherzolite, *Contributions to Mineralogy and Petrology*, *138*(3), 237–248, doi:10.1007/s004100050560.

Klitzsch, E. (1968), Der Basaltvulkanismus des Djebel Haroudj, Ostfezzan, Libya., *Geologische Rundschau*, *57*, 585–601.

Klöcking, M., N. J. White, J. Maclennan, D. McKenzie, and J. G. Fitton (2018), Quantitative Relationships Between Basalt Geochemistry, Shear Wave Velocity, and Asthenospheric Temperature Beneath Western North America, *Geochemistry, Geophysics, Geosystems*, *19*, 3376–3404.

Kogiso, T., T. Kogiso, M. M. Hirschmann, and D. J. Frost (2001), Partial melting experiments of Mg-rich garnet clinopyroxenite and the origin of HIMU basalts, in *AGU Spring Meeting Abstracts*.

Kogiso, T., M. M. Hirschmann, and D. J. Frost (2003), High-pressure partial melting of garnet pyroxenite: possible mafic lithologies in the source of ocean island basalts, *Earth and Planetary Science Letters*, *216*(4), 603–617.

Langmuir, C. H., E. M. Klein, and T. Plank (1992), Petrological systematics of mid-ocean ridge basalts: Constraints on melt generation beneath ocean ridges, *Mantle Flow and Melt Generation at Mid-Ocean Ridges*, *71*, 183–280.

Le Maitre, R. W. (2002), *Igneous Rocks. A Classification and Glossary of Terms. Recommendations of the International Union of Geological Sciences Subcommission on the Systematics of Igneous Rocks*, 2nd ed., 236 pp., Cambridge University Press, Cambridge.

Lee, C. T. A., W. P. Leeman, D. Canil, and Z. X. A. Li (2005), Similar V/Sc systematics in MORB and arc basalts: Implications for the oxygen fugacities of their mantle source regions, *Journal of Petrology*, *46*(11), 2313–2336, doi:10.1093/petrology/egi056.

Lee, C. T. A., P. Luffi, T. Plank, H. Dalton, and W. P. Leeman (2009), Constraints on the depths and temperatures of basaltic magma generation on Earth and other terrestrial planets using new thermobarometers for mafic magmas, *Earth and Planetary Science Letters*, *279*(1-2), 20–33, doi:10.1016/j.epsl.2008.12.020.

Less, G., S. M. Turki, S. K. Suwesi, L. F. Peregi, L. Koloszar, J. Kalmar, K. Sherif, G. Csaszar, Z. Gulasci, H. Dalum, and A. Al Tajuri (2006), *Geological Map of Libya 1 : 250.000. Sheet : Waw Al Kabir NG 33-12. Explanatory Booklet.*, 295 pp., Tripoli.

Lustrino, M., and M. Wilson (2007), The circum-Mediterranean anorogenic Cenozoic igneous province, *Earth-Science Reviews*, *81*(1-2), 1–65, doi: 10.1016/j.earscirev.2006.09.002.

Lustrino, M., C. Cucciniello, L. Melluso, C. C. G. Tassinari, R. dè Gennaro, and M. Serracino (2012), Petrogenesis of Cenozoic volcanic rocks in the NW sector of the Gharyan volcanic field, Libya, *Lithos*, *155*, 218–235, doi:10.1016/j.lithos.2012.09.003.

Macgregor, I. D. (1970), The effect of CaO, Cr_2O_3, Fe_2O_3 and Al_2O_3 on the stability of spinel and garnet peridotites, *Physics of the Earth and Planetary Interiors*, *3*(C), 372–377, doi:10.1016/0031-9201(70)90077-4.

Maclennan, J., and B. Lovell (2002), Control of regional sea level by surface uplift and subsidence caused by magmatic underplating of Earth's crust, *Geology*, *30*(8), 675–678.

Masoud, A. (2014), Composition and age of Cenozoic volcanism in Libya, Ph.D. thesis, Scottish Universities Environmental Research Council, Glasgow University.

McDonough, W. F., and S. S. Sun (1995), The composition of the Earth, *Chemical Geology*, *120*(3-4), 223–253, doi:10.1016/0009-2541(94)00140-4.

McKenzie, D. (2003), Estimating T_e in the presence of internal loads, *Journal of Geophysical Research: Solid Earth*, *108*(B9), 2438, doi:10.1029/2002JB001766.

McKenzie, D. (2010), The influence of dynamically supported topography on estimates of T_e, *Earth and Planetary Science Letters*, *295*(1-2), 127–138, doi: 10.1016/j.epsl.2010.03.033.

McKenzie, D., and M. J. Bickle (1988), The volume and composition of melt generated by extension of the lithosphere, *Journal of Petrology*, *29*(3), 625–679, doi: 10.1093/petrology/29.3.625.

McKenzie, D., and D. Fairhead (1997), Estimates of the effective elastic thickness of the continental lithosphere from Bouguer and free air gravity anomalies, *Journal of Geophysical Research*, *102*(B12), 27,523–27,552, doi:10.1029/97JB02481.

McKenzie, D., and R. K. O'Nions (1991), Partial Melt Distributions From Inversion of Rare-Earth Element Concentrations, *Journal of Petrology*, *32*(5), 1021–1091.

McKenzie, D., J. Roberts, and N. Weiss (1973), Numerical models of convection in the earth's mantle, *Tectonophysics*, *19*(2), 89–103, doi:10.1016/0040-1951(73)90034-6.

McNab, F., P. W. Ball, M. J. Hoggard, and N. J. White (2018), Neogene uplift and magmatism of anatolia: Insights from drainage analysis and basaltic geochemistry, *Geochemistry, Geophysics, Geosystems*, *19*(1), 175–213.

Michael, P. (1995), Regionally distinctive sources of depleted MORB: Evidence from trace elements and H_2O, *Earth and Planetary Science Letters*, *131*(3-4), 301–320, doi:10.1016/0012-821X(95)00023-6.

Miller, C., a. Zanetti, M. Thöni, J. Konzett, and U. Klötzli (2012), Mafic and silica-rich glasses in mantle xenoliths from Wau-en-Namus, Libya: Textural and geochemical evidence for peridotite-melt reactions, *Lithos*, *128-131*, 11–26, doi:10.1016/j.lithos.2011.11.004.

Nataf, H.-C., and Y. Ricard (1996), 3SMAC: an a priori tomographic model of the upper mantle based on geophysical modeling, *Physics of the Earth and Planetary Interiors*, *95*(1-2), 101–122, doi:10.1016/0031-9201(95)03105-7.

Németh, K., S. K. Suwesi, Z. Peregi, Z. Gulácsi, and J. Ujszászi (2003), Plio/Pleistocene Flood Basalt Related Scoria and Splatter Cones, Rootless Lava Flows, and Pit Craters, Al Haruj Al Abiyad, Libya, *GeoLines*, *15*, 98–103.

Nielsen, R. L. (1985), EQUIL: a program for the modeling of low-pressure differentiation processes in natural mafic magma bodies, *Computers & Geosciences*, *11*(5), 531–546.

Nixon, S. (2011), Intra-plate magmatism of the Al Haruj volcanic field, Libya, Ph.D. thesis, University of Cambridge.

Nyblade, A. A., I. Suleiman, F. R. Robert, B. Pursell, A. Suleiman, I. D. Diane, and G. R. Keller (1996), Terrestrial heat flow in the Sirt Basin, Libya, and the pattern, *JoURNAL OF GEOPHYSICAL RESEARCH*, *101*(B8), 17,737–17,746.

Olive, V., R. M. Ellam, and L. Wilson (2001), A protocol for the determination of the rare earth elements at picomole level in rocks by icp-ms: Results on geological reference materials usgs pcc-1 and dts-1, *Geostandards Newsletter*, *25*(2-3), 219–228.

O'Neill, H. S. C., A. J. Berry, C. C. McCammon, K. D. Jayasuriya, S. J. Campbell, and G. Foran (2006), An experimental determination of the effect of pressure on the $Fe_3/\sum Fe$ ratio of an anhydrous silicate melt to 3.0 GPa, *American Mineralogist*, *91*(2-3), 404–412, doi:10.2138/am.2005.1929.

Oun, K. M. (1991), On the poikilitic nature of Jabal Al Hasawinah eudialyte, *Mineralogical Magazine*, *55*(December), 543–547.

Peregi, Z., G. Less, G. Konrád, L. Fodor, Z. Gulácsi, L. Gyalog, S. M. Turki, S. K. Suwesi, K. Sherif, and H. Dulab (2003), *Geological Map of Libya 1:250,000 Sheet Al Haruj al Abyad (NG 33-8). Explanatory Booklet.*, 250 pp., Industrial Research Centre, Tripoli.

Permenter, J. L., and C. Oppenheimer (2007), Volcanoes of the Tibesti massif (Chad, northern Africa), *Bulletin of Volcanology*, *69*(6), 609–626.

Piccoli, G. (1970), Outlines of volcanism in Northern Tripolitania (Libya), *Bulletin of the Geological Society of Italy*, *89*, 449–461.

Pik, R., B. Marty, and D. R. Hilton (2006), How many mantle plumes in Africa? The geochemical point of view, *Chemical Geology*, *226*(3-4), 100–114, doi:10.1016/j.chemgeo.2005.09.016.

Pilet, S., M. B. Baker, O. Müntener, and E. M. Stolper (2011), Monte Carlo simulations of metasomatic enrichment in the lithosphere and implications for the source of alkaline basalts, *Journal of Petrology*, *52*(7-8), 1415–1442, doi:10.1093/petrology/egr007.

Plank, T., and D. W. Forsyth (2016), Thermal structure and melting conditions in the mantle beneath the Basin and Range province from seismology and petrology, *Geochemistry, Geophysics, Geosystems*, *17*(4), 1312–1338, doi:10.1002/2015GC006205.

Press, W. H., B. P. Flannery, S. A. Teukolsky, and W. T. Vetterling (1986), *Numerical Recipes*, Cambridge University Press, Cambridge.

Priestley, K., and D. McKenzie (2006), The thermal structure of the lithosphere from shear wave velocities, *Earth and Planetary Science Letters*, *244*(1-2), 285–301, doi: 10.1016/j.epsl.2006.01.008.

Priestley, K., and D. McKenzie (2013), The relationship between shear wave velocity, temperature, attenuation and viscosity in the shallow part of the mantle, *Earth and Planetary Science Letters*, *381*, 78–91, doi:10.1016/j.epsl.2013.08.022.

Radivojević, M., M. Toljić, S. M. Turki, Z. Bojić, K. Šarić, and V. Cvetković (2015), Neogene to Quaternary basalts of the Jabal Eghei (Nuqay) area (south Libya): Two distinct volcanic events or continuous volcanism with gradual shift in magma composition?, *Journal of Volcanology and Geothermal Research*, *293*, 57–74, doi: 10.1016/j.jvolgeores.2015.02.003.

Richards, F. D., M. J. Hoggard, L. Cowton, and N. J. White (2018), Reassessing the Thermal Structure of Oceanic Lithosphere With Revised Global Inventories of Basement Depths and Heat Flow Measurements, *Journal of Geophysical Research: Solid Earth*, *123*, 9136–9161.

Roden, M. K., S. R. Hart, F. A. Frey, and W. G. Melson (1984), Sr, Nd and Pb isotopic and REE geochemistry of St. Paul's Rocks: the metamorphic and metasomatic development of an alkali basalt mantle source, *Contributions to Mineralogy and Petrology*, *85*, 376–390.

Roex, A. P., A. Späth, and R. E. Zartman (2001), Lithospheric thickness beneath the southern Kenya Rift: implications from basalt geochemistry, *Contributions to Mineralogy and Petrology*, *142*(1), 89–106, doi:10.1007/s004100100273.

Roohi, M. (1996), Geological history and hydrocarbon migration pattern of the As Zaahra-Al Hufrah platform, *The geology of the Sirt Basin: Amsterdam, Elsevier*, *1*, 195–232.

Rudge, J. F., G. G. Roberts, N. J. White, and C. N. Richardson (2015), Uplift histories of Africa and Australia from linear inverse modeling of drainage inventories, *Journal of Geophysical Research F: Earth Surface*, *120*(5), 894–914, doi:10.1002/2014JF003297.

Schaeffer, A. J., and S. Lebedev (2013), Global shear speed structure of the upper mantle and transition zone, *Geophysical Journal International*, *194*(1), 417–449, doi: 10.1093/gji/ggt095.

Schult, A., and H. Soffel (1973), Palaeomagnetism of Tertiary Basalts from Libya, *Geophysical Journal of the Royal Astronomical Society*, *32*(3), 373–380, doi:10.1111/j.1365-246X.1973.tb05837.x.

Shorttle, O., and J. Maclennan (2011), Compositional trends of Icelandic basalts: Implications for short-length scale lithological heterogeneity in mantle plumes, *Geochemistry, Geophysics, Geosystems*, *12*(11), doi:10.1029/2011GC003748.

Späth, A., A. P. Le Roex, and N. Opiyo-Akech (2001), plume-lithosphere interaction and the origin of continental rift-related alkaline volcanism - the Chyulu hills volcanic province, southern Kenya, *Journal of Petrology*, *42*(4), 765–787.

Steinberger, B. (2000), Plumes in a convecting mantle: Models and observations for individual hotspots, *Journal of Geophysical Research: Solid Earth*, *105*(B5), 11,127–11,152.

Stracke, A., A. W. Hofmann, and S. R. Hart (2005), Fozo, himu, and the rest of the mantle zoo, *Geochemistry, Geophysics, Geosystems*, *6*(5).

Suayah, I. B., J. S. Miller, B. V. Miller, T. M. Bayer, and J. J. W. Rogers (2006), Tectonic significance of Late Neoproterozoic granites from the Tibesti massif in southern Libya inferred from Sr and Nd isotopes and U-Pb zircon data, *Journal of African Earth Sciences*, *44*(4-5 SPEC. ISS.), 561–570, doi:10.1016/j.jafrearsci.2005.11.020.

Takahashi, E., T. Shimazaki, Y. Tsuzaki, and H. Yoshida (1993), Melting study of a peridotite klb-1 to 6.5 gpa, and the origin of basaltic magmas, *Phil. Trans. R. Soc. Lond. A*, *342*(1663), 105–120.

Takei, Y. (2017), Effects of Partial Melting on Seismic Velocity and Attenuation: A New Insight from Experiments, *Annual Review of Earth and Planetary Sciences*, *45*(1), 447–

470, doi:10.1146/annurev-earth-063016-015820.

Tanaka, T., S. Togashi, H. Kamioka, H. Amakawa, H. Kagami, T. Hamamoto, M. Yuhara, Y. Orihashi, S. Yoneda, H. Shimizu, T. Kunimaru, K. Takahashi, T. Yanagi, T. Nakano, H. Fujimaki, R. Shinjo, Y. Asahara, M. Tanimizu, and C. Dragusanu (2000), JNdi-1: a neodymium isotopic reference in consistency with LaJolla neodymium, *Chemical Geology*, *168*, 279–281.

Thompson, R. N., C. J. Ottley, P. M. Smith, D. G. Pearson, A. P. Dickin, M. A. Morrison, P. T. Leat, and S. A. Gibson (2005), Source of the quaternary alkalic basalts, picrites and basanites of the Potrillo Volcanic Field, New Mexico, USA: Lithosphere or convecting mantle?, *Journal of Petrology*, *46*(8), 1603–1643, doi:10.1093/petrology/egi028.

Varne, R. (1970), Hornblende lherzolite and the upper mantle, *Contributions to Mineralogy and Petrology*, *27*(1), 45–51.

Vincent, P. (1970), The evolution of the Tibesti volcanic province, eastern Sahara, in *African magmatism and tectonics*, pp. 301–319, Oliver and Boyd Edinburgh.

Wacrenier, P., H. Hudeley, and P. Vincent (1958), *Notice explicative de la carte géologique provisoire du Borkou-Ennedi-Tibesti au 11/. 000.000*, Afrique équatoriale française, Haut Commissariat de la république, Direction des mines et de la géologie.

Wessel, P., and W. H. F. Smith (1991), Free software helps map and display data, *Eos, Transactions American Geophysical Union*, *72*(41), 441–446.

White, R. S., D. M^{c}Kenzie, and R. K. O'Nions (1992), Oceanic Crustal Thickness From Seismic Measurements and Rare Earth Element Inversions, *Journal of Geophysical Research*, *97*, 19,683–19,715.

Williams, A., F. Stuart, S. Day, and W. Phillips (2005), Using pyroxene megaphenocrysts to determine cosmogenic 3He concentrations in old volcanic rocks: an example of landscape development in central Gran Canaria, *Quaternary Science Reviews*, *24*, 211–222.

Yamauchi, H., and Y. Takei (2016), Polycrystal anelasticity at near-solidus temperatures, *Journal of Geophysical Research: Solid Earth*, *121*(11), 7790–7820, doi:10.1002/2016JB013316.

Yaxley, G. M., and D. H. Green (1998), Reactions between eclogite and peridotite: mantle refertilisation by subduction of oceanic crust, *Schweiz. Mineral. Petrogr. Mitt*, *78*(2), 243–255.

Zindler, A., and S. Hart (1986), Chemical geodynamics, *Annual review of earth and planetary sciences*, *14*(1), 493–571.